

THESIS FOR DEGREE OF DOCTOR OF PHILOSOPHY

**Powder degradation during powder bed fusion processing:
impact of processing conditions and alloy composition**

AHMAD RAZA



Department of Industrial and Materials Science
CHALMERS UNIVERSITY OF TECHNOLOGY

Gothenburg, Sweden, 2022

Powder degradation during powder bed fusion processing: impact of processing conditions and alloy composition

Ahmad Raza

ISBN: 978-91-7905-748-0

©Ahmad Raza, 2022

Doktorsavhandlingar vid Chalmers tekniska högskola

Ny serie nr 5214

ISSN0346-718X

Department of Industrial and Materials Science

Chalmers University of Technology

SE-412-96 Gothenburg

Sweden

Tel: +46 (0)31-772 1271

Email: ahmadra@chalmers.se

Printed by Chalmers Reproservice

Gothenburg, Sweden 2022

Abstract

In the recent decade, powder bed fusion (PBF) metal additive manufacturing (AM) has attracted huge attention both from the industry and the research community. This effort has helped mature PBF technology as a potential alternative to conventional manufacturing processes as casting, machining, forging, etc. However, there remain various challenges hindering the path of large-scale adoption of these techniques in the manufacturing industry. One such challenge affecting the cost, reproducibility of the products and sustainability of the process, is the reusability of unconsumed powder after each build job. The issue during powder reusability is the likelihood of degraded quality of the reused powder compared to virgin powder either by oxidation during exposure to the atmosphere, or accumulation of process byproducts, referred to as spatters, during processing. The quality degradation of the feedstock powder can lead to an increased number of defects in the produced products and affect the robustness and reproducibility of the PBF process. This thesis is focused on determining the dominant powder degradation mechanisms in powder bed fusion laser-beam (PBF-LB) and powder bed fusion electron-beam (PBF-EB) processes. Here, the approach to investigate the degradation of reused powder is based on the dedicated analysis of changes in powder surface chemistry, analysis of oxygen pick-up, and variation in surface morphology.

During the analysis of the powders during the PBF-LB process, three different alloy systems were studied, namely aluminum alloys (AlSi10Mg), nickel-based superalloys (Alloy 718 and Hastelloy X (HX)), and titanium alloys (TiAl6V4). The assessment of powder degradation was initiated with the investigation of AlSi10Mg powder reused for over 30 months. The analysis showed that the powder degradation is mainly triggered by the accumulation of highly oxidized spatter particles in the powder, characterized by the overall greater oxide layer thickness (~75-125 nm) on the surface of powder. These oxidized spatter particles are contributing towards increasing the oxygen content and number of defects in the as-printed components. Analysis of the surface oxide state of spatter particles, generated during the processing of Alloy 718, HX alloy, and TiAl6V4 revealed that the extent of oxidation of spatters from different alloy systems is dependent on the content of oxidation-sensitive elements e.g., Al, Ti, Cr, etc. The impact of the part design in terms of surface to volume ratio of the part on the spatter generation and accumulation was also shown. Results also show an increasing amount of spatter formation with increasing layer thickness per layer deposited. However, the total amount of spatter generated per build job is lower when a higher layer thickness was applied. The results have shown that by employing appropriate processing gas composition containing He the generation of spatter can be reduced. Furthermore, by reducing residual oxygen content in the build chamber, the extent of spatter oxidation can be reduced. Finally, the effect of powder degradation on the quality of fabricated parts was analyzed where the accumulation and redeposition of spatters on the powder bed resulted in a lack of fusion defects, higher porosity, and a decrease in the strength of fabricated parts.

In the PBF-EB process, powder oxidation and sublimation of volatile elements during the processing of Alloy 718 have been investigated. The results have identified powder oxidation during PBF-EB processing, due to the long-term powder exposure to high temperature, as the dominant powder degradation mechanism. Furthermore, the sublimation of the alloying elements such as Al and Cr in the case of PBF-EB processing of Alloy 718 was detected.

Keywords: additive manufacturing; powder bed fusion - laser beam; powder bed fusion – electron beam; AlSi10Mg; Alloy 718; powder degradation; oxidation; spatter particles; residual oxygen; sublimation; TiAl6V4, Hastelloy X.

Preface

The work presented in this doctoral thesis was conducted at the Division of Materials and Manufacture, within the Department of Industrial and Materials Science, at Chalmers University of Technology. The work was conducted in the framework of the Centre for Additive Manufacturing – Metal (CAM²). The research was directly supervised by Prof. Eduard Hryha, and Prof. Lars Nyborg was the examiner.

List of appended papers

- I. Degradation of AlSi10Mg Powder during Laser-Based Powder Bed Fusion Processing**
Ahmad Raza, Tobias Fiegl, Imran Hanif, Andreas Markström, Martin Franke, Carolin Körner, Eduard Hryha
Materials & Design 198(2021) 109358
<https://doi.org/10.1016/j.matdes.2020.109358>
- II. Spatter formation during Laser Powder Bed Fusion of Inconel 718 alloy monitored by Optical Tomography**
Zhuoer Chen, Ahmad Raza, Eduard Hryha
Journal of Manufacturing Processes
<https://doi.org/10.1016/j.jmapro.2022.07.031>
- III. Oxygen balance during laser powder bed fusion of Alloy 718**
C. Puzon, Ahmad Raza, E. Hryha, P. Forêt
Materials & Design 201(2021) 109511
<https://doi.org/10.1016/j.matdes.2021.109511>
- IV. Effect of layer thickness on spatters oxidation of HX alloy during powder bed fusion-laser beam processing**
Ahmad Raza, Claudia Schwerz, Camille Puzon, Lars Nyborg, Eduard Hryha
Manuscript
- V. Effect of layer thickness on spatter properties during laser powder bed fusion of Ti-6Al-4V**
Ahmad Raza, Camille Puzon, Sophie Dubiez Le Goff, Eduard Hryha
Submitted for Journal Publication
- VI. Effect of processing gas on spatter generation and oxidation of TiAl6V4 Alloy in laser powder bed fusion process**
Ahmad Raza, Camille Puzon, Sophie Dubiez Le Goff, Eduard Hryha
Submitted for journal publication
- VII. Spatter oxidation during laser powder bed fusion of Alloy 718 in dependence on oxygen content in the process atmosphere**
Ahmad Raza, C. Puzon, E. Hryha, Andreas Markström, P. Forêt
Additive Manufacturing
<https://doi.org/10.1016/j.addma.2021.102369>
- VIII. In-situ detection of redeposited spatter and its influence on the formation of internal flaws in laser powder bed fusion**
Claudia Schwerz, Ahmad Raza, Xiangyu Lei, Lars Nyborg, Eduard Hryha, Håkan Wirdelius
Additive Manufacturing

<https://doi.org/10.1016/j.addma.2021.102370>

IX. Effect of AlSi10Mg0.4 long-term reused powder in PBF-LB/M on the mechanical properties

Tobias Fiegl, Martin Franke, Ahmad Raza, Eduard Hryha, Carolin Körner
Materials and Design

<https://doi.org/10.1016/j.matdes.2021.110176>

X. Rheological Behavior of Inconel 718 Powder for Electron-Beam Melting

Laura Cordova, Ahmad Raza, Eduard Hryha
Metals

<https://doi.org/10.3390/met12071231>

XI. Characterization of spatter and metallization in 718 alloys during the electron beam melting process

Ahmad Raza, Eduard Hryha
Materials

<https://doi.org/10.3390/ma14205953>

Contribution to the appended papers

I, XI: The author planned and conducted the experiments in collaboration with co-authors and wrote the paper in collaboration with coauthors. The co-authors helped with sample collection, TEM and Thermo-calc analysis, and reviewing the articles.

II: The author planned the experiment with the collaboration of co-authors. The author did the SEM and XPS analysis, analyzed the results, and wrote the part of the paper. Z. Chen printed and analyzed OT data and took the lead in writing the paper.

IV: The author planned and conducted the experiments in collaboration with co-authors. The author did the SEM and XPS analysis and analyzed the results. The Optical tomography (OT) analysis was conducted by C. Schwerz. The writing was done in collaboration with co-authors.

III: The author planned the experiments with the collaboration of a co-author as an extension of paper I. The author did the powder's fractography and surface analysis and contributed to this part's writing. The co-author, Tobias Fiegl, did the rest of the experimental work and writing in this paper. The reason for appending this paper is to provide context for paper I.

III, V, VI, VII: The author planned and conducted the experiments in collaboration with co-authors. The author did the XPS analysis and analyzed the results. The SEM analysis was conducted by C. Pauzon. The writing was done in collaboration with co-authors.

VIII: The author planned and conducted the experiments in collaboration with co-authors. This study was led by Co-author (C. Schwerz) who printed and collected the samples. The author contributed with the SEM, XPS, and fractography analysis and analyzed the results. The writing was done in collaboration with co-authors.

X: The author planned and conducted the experiments in collaboration with co-authors. The author did the XPS analysis and analyzed the results. The flowability analysis was conducted by L. Cordova. The writing was done in collaboration with co-authors.

ABBREVIATIONS

AM	Additive Manufacturing
BSE	Backscattered Electrons
CAD	Computer-Aided Design
CCD	Charge-Coupled Device
EBM	Electron Beam Belting
PBF-EB	Powder Bed Fusion - Electron Beam
EDS	Energy Dispersive Spectroscopy
HR-SEM	High-Resolution Scanning Electron Microscopy
ALLOY 718	Inconel 718, Alloy 718
PBF-LB	Powder Bed Fusion – Laser Beam
PM	Powder Metallurgy
PBF	Powder Bed Fusion
PSD	Particle Size Distribution
RQ	Research Question
SE	Secondary Electron
STL	Stereo-Lithography
STEM	Scanning Transmission Electron Microscopy
XPS	X-ray Photoelectron Spectroscopy
Nano-SIMS	Nano Secondary Ions Mass Spectroscopy

Table of Contents

1	Introduction	1
1.1	Background	1
1.1	Research objectives	2
1.2	Research Strategy	2
2	Powder bed fusion techniques	5
2.1	Powder bed fusion-laser beam (PBF-LB)	5
2.2	Powder bed fusion-electron beam (PBF-EB).....	6
3	Powders for Additive Manufacturing	9
3.1	Powder manufacturing methods.....	9
3.2	Inert gas atomization	10
3.3	Electrode induction gas atomization	10
3.4	Plasma atomization process	12
3.5	Plasma rotating electrode process	13
3.6	Powder properties for additive manufacturing.....	13
3.6.1	Morphology	14
3.6.2	Powder size distribution	15
3.6.3	Density.....	15
3.6.4	Rheology.....	15
3.6.5	Chemistry.....	16
3.6.6	Variation in powder properties with reusability	16
4	Powder degradation in PBF processes	19
4.1	Oxidation of metals	19
4.1.1	Thermodynamics of oxidation	19
4.2	Powder degradation in PBF-LB	20
4.2.1	Feedstock powder oxidation by atmospheric exposure	20
4.2.2	Spatter formation and accumulation in reused powder	21
4.3	Powder degradation in the PBF-EB process	22
4.3.1	Sublimation of metallic elements during PBF-EB	24
5	Materials	27
5.1	Aluminum alloys	27
5.1.1	Additive Manufacturing of Aluminum alloys.....	27
5.2	Nickel-based superalloys	28
5.2.1	Additive manufacturing of superalloys.....	28
5.3	Titanium alloys.....	28
5.3.1	Additive manufacturing of Ti Alloys.....	29

6	Experimental Methods	31
6.1	Materials and processing.....	31
6.1.1	PBF-LB processing of AlSi10Mg	31
6.1.2	PBF-LB Processing of Alloy 718.....	32
6.1.3	PBF-LB Processing of Hastelloy X	33
6.1.4	PBF-LB Processing of TiAl6V4	34
6.1.5	PBF-EB processing of Alloy 718	34
6.2	Characterization techniques	35
6.2.1	Bulk chemical analysis.....	35
6.2.2	Microscopy.....	35
6.2.3	Surface analysis	38
7	Results & Discussion	43
7.1	Summary of research questions.....	43
7.2	Summary of appended papers	44
8	Conclusions	57
9	Future work	59
10	Acknowledgements	61
11	References	63

1 Introduction

1.1 Background

In the late 19th century, the first alternative to subtractive manufacturing appeared in the form of powder metallurgy (PM) where metallic powders were used to fabricate the products [1,2]. Conventional powder metallurgy is governed by a press and sinter route where metallic powder is pressed under high mechanical pressure and sintered at elevated temperatures in a controlled atmosphere. Over the years, several stages of the PM processing route have been developed, which include powder forging, hot isotactic pressing, spark plasma sintering, metal injection molding, etc.[2–6]. With the dawn of the 21st century and advancements in computational technology, a new set of techniques based on additive manufacturing (AM) “3D printing” has emerged where metallic powder is used [7]. Due to their capability to fabricate complex geometries conventionally impossible, the AM processes are getting popular both in the industries and the research community [8].

Among powder-based AM techniques, the powder bed fusion laser beam (PBF-LB) and powder bed fusion electron beam (PBF-EB) have captured an 85 % share of the AM industry, according to AM POWER report 2022 [9]. Moreover, as per the AMPOWER report 2022, the PBF-LB has achieved a maturity index where it is ready for widespread industrial use [9]. The PBF techniques work on the layer-by-layer addition principle where the laser/electron beam scans the designed part after the spread of each powder layer [10]. In terms of consumption of feedstock powder, PBF techniques are quite different from conventional PM techniques. In conventional PM techniques, powder usage is efficient, and the process does not result in any leftover powder after the fabrication of the part. However, for the PBF techniques, not all the powder gets consumed and a large quantity of the powder from the powder bed, typically above 40%, is left over [11–13]. Although the cost of powder feedstock is <10% of the overall cost of AM products at the current state-of-the-art [9], the reusability of unconsumed powder is crucial for sustainability and economic reasons.

Currently, researchers and high-end industries (aerospace, etc.) rely on using virgin powder for the fabrication of the parts as well as process development for different materials. The reason behind not reusing leftover powder relates to the potential degradation of the powder during the prior build process. The extent of powder degradation depends on the PBF process, process parameters, process atmosphere, handling of the powder, etc. [14–17]. In terms of the PBF process, the PBF-EB operates at significantly higher temperatures and vacuum conditions compared to the PBF-LB process, which instead works in nearly ambient conditions and in an inert atmosphere. Such variation in processing conditions will affect the powder quality differently [18]. Similarly, variations in process parameters like layer thickness, laser power, and hatch spacing can affect the number of process byproducts which can eventually influence the quality of leftover powder as well as fabricated parts [19]. In addition, the type of the process atmosphere and its purity plays a significant role in controlling the rate of powder degradation [20,21].

For the reusability of powders, a comprehensive understanding of the powder degradation mechanism is essential. To date, there have been plenty of investigations related to the effect of powder degradation on flowability, powder size distribution (PSD), shape and morphology of the powder [22–25]. However, these are not the only aspects that measure and standardize

the quality of the reused powder. There is a need for a dedicated study on the chemistry aspects of powder degradation where variation in both, bulk and surface chemistry should be monitored. Also, the effect of different PBF processes and processing conditions on the chemistry aspect of powder degradation needs to be monitored.

To date, there are few research studies analyzing the impact of powder reuse on the level of oxidation, therefore knowledge of the mechanisms involved in powder deterioration during AM is limited. This thesis focuses on identifying the mechanisms of powder and spatter oxidation utilizing cutting-edge surface characterization backed by thermodynamics modeling.

1.1 Research objectives

The goal of this thesis study is to understand the underlying mechanisms of powder degradation during PBF processing in correlation to alloy composition. Moreover, the effect of part geometry, processing parameters (powder layer thickness), processing gas and its purity on spatter formation and oxidation has been evaluated. Finally, the effect of powder degradation on the properties of the produced parts is evaluated. Four materials were covered in this thesis: AlSi10Mg, TiAl6V4, Alloy 718, and Hastelloy X. To address these issues, an effort has been made to answer the following research questions (RQ):

RQ1: What is the dominant powder degradation mechanism in the PBF-LB process and how does it depend on alloy composition?

RQ2: What is the effect of part geometry and processing parameters on the generation and properties of spatter during PBF-LB?

RQ3: What is the effect of powder degradation on the properties of fabricated parts?

RQ4: What is the dominant powder degradation mechanism in the PBF-EB process?

1.2 Research Strategy

Powder degradation can be defined in different ways depending on the aspect of powder characteristics such as rheology, density, morphology, and chemistry. The focus of this thesis is on the chemistry aspects of powder where the bulk and surface chemistry of the powders is evaluated. The chemistry of the virgin powder was taken as the benchmark and the extent of powder degradation of reused powder was determined by comparing with virgin powder.

The goal of this thesis study is to enhance the understanding of the powder degradation mechanism in the PBF-LB process and the PBF-EB process where this work can be divided into two parts. The first part addressing RQ1, RQ2, and RQ3 is concerning the research done related to the PBF-LB process. The second part includes RQ4 which is focused on the PBF-EB process. The appended papers in this thesis and their connection with the research questions have been summarized in Table 1.

The RQ1 consists of two parts where the first part concerns the determination of the dominant powder degradation mechanism in the PBF-LB process. This has been done by a study on AlSi10Mg (paper I) where the powder was processed over 30 months (5000 machine hours). To relate the findings regarding the dominant degradation mechanism with other materials, the powders from Alloy 718 (Papers II and III), HX alloy (Paper IV) and TiAl6V4 (Paper V) were investigated. Once a dominant powder degradation mechanism in the PBF-LB process was

established, for further addressing RQ2 different design and processing parameters were varied to evaluate their effect on powder degradation. The effect of part geometry and design on the degradation is presented in paper III, where the capsules with varying lattice structures were fabricated and their effect on the properties of the powder was examined. Regarding the process parameters, the effect of powder layer thickness (Papers IV, and V), processing gas (paper VI), and atmospheric purity (Paper VII) has been examined. Finally, the impact of powder degradation in the PBF-LB process on the properties of fabricated parts were investigated where findings are presented in papers VIII and IX.

The second part of the thesis concerns the PBF-EB process (RQ4) where an investigation of dominant powder degradation mechanisms in the PBF-EB process has been conducted. In the first part (paper X), the oxidation of alloy 718 during the PBF-EB process has been investigated. This has been supplemented with another study focused on the sublimation of volatile elements during the processing of alloy 718 in the harsh high temperature and vacuum condition of the PBF-EB process (Paper XI).

Table 1: The summary of appended papers and their connection with the research questions.

	RQ1	RQ2	RQ3	RQ4	Material
Paper I					AlSi10Mg
Paper II					Alloy 718
Paper III					Alloy 718
Paper IV					HX Alloy
Paper V					TiAl6V4
Paper VI					TiAl6V4
Paper VII					Alloy 718
Paper VIII					HX Alloy
Paper IX					AlSi10Mg
Paper X					Alloy 718
Paper XI					Alloy 718

2 Powder bed fusion techniques

The advanced manufacturing process known as additive manufacturing (AM), sometimes referred to as "3-dimensional (3D) printing", involves building an object layer by layer in an additive manner [25]. It is a step in the right direction for the manufacturing sector's digitalization. Before the design is introduced into AM machines and printing, several computational prefabrication stages are conducted, and this is where the digitalization part comes from [26]. First, a computer-aided design (CAD) model that includes 2D and 3D visuals of the component is used to create the design of the component. The STL (stereo lithography) file, which is a triangular representation of the design's surface geometry, is created from the CAD file [7]. Before being sent to the machine, the resulting STL file is further processed in compatible AM software to provide workable printing settings. The information on the design, orientation, build direction, support structure, material, and process parameters (layer thickness, power, etc.) is then introduced to the machine as a machine-readable file. Depending on the technology used in the AM, the process parameters can change. Once all these computing operations have been completed, the machine obeys the directions and prints the intended product on its own.

The ISO/ASTM 52900-2021 standard for AM specifies seven categories in which AM technology can be classified. Among those seven types of AM processes, three AM processes employ powder as a feedstock and are termed powder bed fusion (PBF), binder jetting (BJT), and directed energy deposition (DED) [27]. This thesis is focused on investigating the characteristics of PBF processes.

The PBF is one of the most used AM processes. The PBF process employs an energy source to melt powder feedstock into the designed pattern layer by layer. Depending on the energy source, the PBF process can be separated into two distinct methods: powder bed fusion – electron beam (PBF-EB), in which the powder layer is melted using an electron beam, and powder bed fusion – laser beam (PBF-LB), in which the powder layer is melted using a laser. The parts that follow briefly discuss the fundamentals of both processes.

2.1 Powder bed fusion-laser beam (PBF-LB)

The PBF-LB machine's operating principle is rather basic. Figure 1 shows a schematic of the machine. The powder dispenser, building area and powder collector are the machine's three main powder-related sections. By filling the powder dispenser, the powder is put into the machine. A recoater spreads a layer of powder into the build area after a certain oxygen level is attained there. The excess powder is raked up and placed in the powder collector. The piston at the system's bottom regulates the amount of powder accessible and controls how much powder flows from the dispenser. A piston at the base of the build area also controls the layer thickness. An optical system is used to change the laser beam's location. Following the component design, the laser scans the build plate after the powder has been dispersed around the build area. The build cycle is then completed by repeating this process, layer by layer.

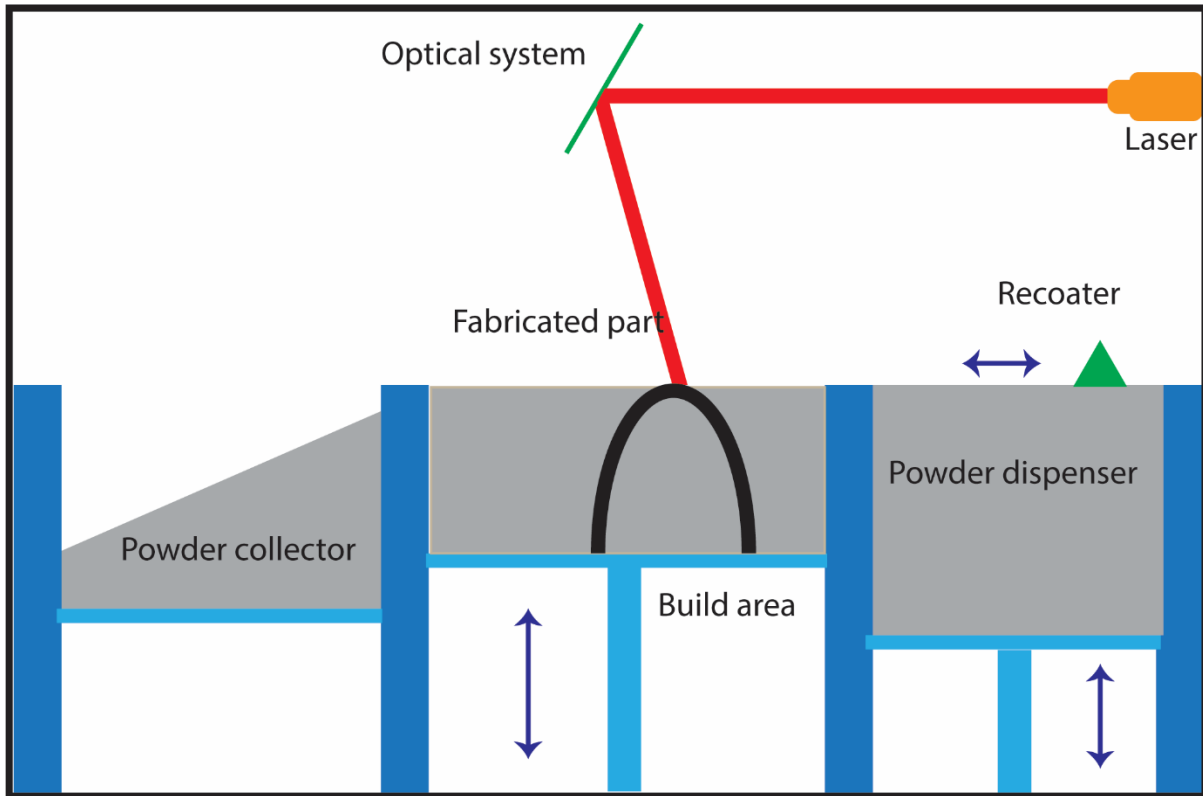


Figure 1: A schematic depiction of the PBF-LB process.

After the build cycle is finished, the leftover powder is removed using a powder extraction module and is further sieved to remove spatters and other debris before reuse. The required powder size distribution (PSD) of virgin powder determines the size of the used sieve and sieving process. The build platform is removed from the machine for post-processing once the powder has been removed. During post-process, various operations, such as support removal, machining, surface treatment, etc., are commonly included. For the qualities of produced components to be repeatable, the post-processing uniformity after each build job is crucial. Additionally, several additional factors, including powder quality, powder size distribution (PSD), laser power, layer thickness, hatch distance, scan speed, scan strategy, gas flow rate, etc., can significantly affect the attributes of produced components. To achieve the repeatability of PBF-LB products, these factors must be carefully controlled.

2.2 Powder bed fusion-electron beam (PBF-EB)

In contrast to PBF-LB, the PBF-EB is an AM method that allows the manufacture of multilayer components without the need for support structures. A schematic of a PBF-EB machine with hoppers on either side of the construction area is shown in Figure 2. After each printing cycle, the powder is taken from hoppers and dispersed in the build area using a recoater [28]. As implied by the name, the heat source is an electron beam, and electromagnetic lenses are used to alter the beam's direction. The PBF-EB method is much quicker than the PBF-LB technique because of electromagnetic lenses' beam control. Ultrahigh vacuum ($\sim 10^{-6}$ bar), a requirement for the PBF-EB process, is necessary to achieve high energy efficiency [29].

There are two processes involved in scanning the powder bed with an electron beam. The entire powder bed is pre-heated in the first phase so that the powder can be partially sintered. This is done to improve the conductivity of the powder bed. Due to the un-sintered powder's low

powder bed conductivity, which can lead to an electron buildup, the smoking effect — also known as the ejection of powder from the powder bed by repulsion before melting — can occur. In addition to preventing the smoking effect, semi-sintering powder at a high temperature has other advantages. Support structures can be eliminated or reduced since the sintered powder acts as support. It also enables the prevention of the production of residual stresses. The second stage involves the system increasing the beam intensity to melt the sintered powder bed while a high-energy electron beam selectively scans the planned item. Up until the manufactured part's construction height is attained, this process is repeated.

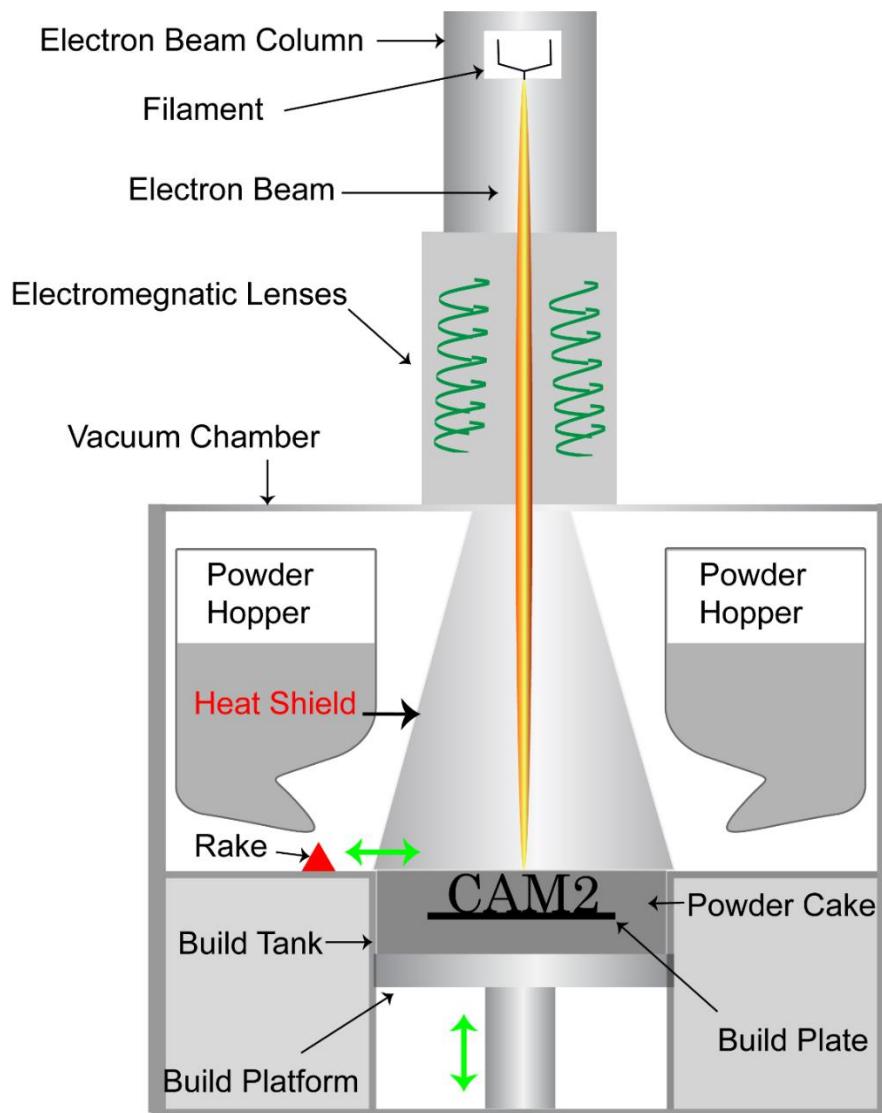


Figure 2: A schematic drawing of the PBF-EB process.

To prevent powder from oxidizing once a build cycle is finished, the machine must cool down before the chamber can be opened. The build platform with the powder cake is taken out of the machine and put in a powder recovery system after cooling. Grit blasting is used to extract the sintered powder from manufactured parts and the cake itself. After sieving, grit blasting helps turn the semi-sintered cake into powder particles for future reuse. Additionally, the recovered components undergo additional post-processing before being applied to the necessary applications.

Although high temperature and high vacuum boost the process stability, the same conditions can also hasten the rate at which powder degrades. In the chapters that follow, these issues are covered in more detail.

3 Powders for Additive Manufacturing

The traditional metal-related sector offers over 5000 alloys and metal systems [30]. Such a broad selection of metallic material possibilities is not currently accessible for AM because the field is still in its infancy. Even with complicated material/process development, using already-developed alloys in additive manufacturing still needs a thorough understanding of how energy sources interact with powder in the built environment. Only 30 metal alloys (PBF, BJ, and DED) are approved for use in powder-based AM processes [30] because of the difficulty of the process development. Although most of the AM materials (shown in Table 2) are derived from traditional alloys, most of the alloys need to have their composition altered to accommodate the AM process's quick melting and solidification. The sophisticated material development for AM technology also includes composition customization.

Table 2: Current list of qualified alloy powders for different AM techniques [30].

AM technology		Alloys	No
PBF	LB-PBF	Al: AlSi10Mg, AlSi7Mg0.6, AlSi9Cu3, AlSi12, Scalmalloy Co: CoCr28Mo6, CoCr24Mo5, CoCr25Mo5W5 Cu: Cu, <u>CuCrZr</u> , Cu-10Sn, CuNi2SiCr Ni: IN625, IN718, IN939, HX Ti: <u>TiCP</u> , Ti6Al4V Stainless steel: 316L, 17-4 PH, 15-5PH Tool steel: CX, PH1, GP1, 20MnCr5, MS1, 1.2709, H13 (1.2344), Invar36 Refractory: W Precious: 18714K Gold (red, yellow, white), 925Si, 95Pt/5Ru	33
	EB-PBF	Ti: Ti, Ti6Al4V Co: CoCr28Mo6 Ni: IN718 <u>Intermetallics</u> : TiAl4822	5
	BJT	Ni: IN625, 247 Ti: Ti6Al4V Stainless steels: 316L, 17-4PH, 304L Tool steels: M2	7
	DED	Ni: IN625, IN718 Ti: Ti6Al4V Stainless steel: 316L	4

Despite the small number of metallic materials available for AM, they span a wide variety of alloys with various compositions, physical characteristics and chemical activities. To produce powder, it is necessary to carefully evaluate the alloy composition as well as the desired chemical and physical qualities of the powder. The AM powder production techniques will be discussed in the sections that follow. Additionally, the necessary set of powder qualities to consider for powder used in AM will be covered.

3.1 Powder manufacturing methods

There are several methods used to create a powder from bulk material and powder production for use in powder metallurgy techniques is a well-established area. These methods include liquid melt disintegration, chemical reduction, electrolytic reduction from solution and

mechanical comminution. The most common industrial method for producing metal powder is called atomization, and it involves physically disintegrating liquid melt [31–34].

Powder fabrication for AM takes extra consideration since factors like form, size, morphology, surface chemistry, rheology, etc., may affect how easily the powder can be processed in the AM machine. For the manufacturing of powder for AM, the following atomization processes are frequently employed:

1. Inert gas atomization
2. Electrode induction gas atomization (EIGA)
3. Plasma atomization process
4. Plasma rotating electrode process

3.2 Inert gas atomization

The most popular atomization method for creating AM powder is gas atomization, which is especially effective for alloys with Fe and Ni bases (Hastelloy X, IN625, Alloy 718, etc.) [35]. Figure 3a presents a graphic representation of this method. The first method (shown in Figure 3a) involves charging virgin raw material into an induction furnace, which then melts the material using eddy currents [33]. The environment in which the furnace is located depends on the alloying components' susceptibility to oxidation. To make up for the heat lost in the next phases, the melt is overheated. The melt is then transferred to a tundish to provide a uniform flow to the atomizer nozzle in the following stage. Once the melt stream has passed the nozzle, it is step-wise broken up into tiny melt droplets by pressurized gas. During their journey, these melt droplets solidify before landing at the bottom of the atomizing chamber. To minimize surface energy during solidification, the droplet's surface tension urges it toward adopting a spherical form.

Two different atomizing nozzle types—the freefall nozzle and the close-coupled nozzle—are frequently employed in this procedure. The size and shape of the generated powder can be affected by the kind of nozzle used. Powder size distribution (PSD) for a close-coupled nozzle is in the range of 5-200 μm , with $D_{50} = 50 \mu\text{m}$. PSD is obtained using a free-fall nozzle between 50 and 300 μm with a D_{50} of 100 μm [30]. Although the close-coupled nozzle generates a narrower range of powder, satellite development on the powder surface is more likely because of the turbulent melt flow in the nozzle.

3.3 Electrode induction gas atomization

In terms of charging technique, electrode induction gas atomization (EIGA) differs from inert gas melting in that a bar with a set composition is melted by induction. Charged bar diameters can reach 150 mm on average. The melt is broken up into tiny droplets as it passes through an atomizing nozzle (see Figure 3b). During their flight, these droplets harden and land at the bottom of the container. The generated powder has a PSD of between 10 and 500 μm and a D_{50} of between 90 and 140 μm . To prevent oxide impurities, this method is more frequently used for alloys containing highly reactive components such as TiAl6V4, TiAl, NiTi, etc.

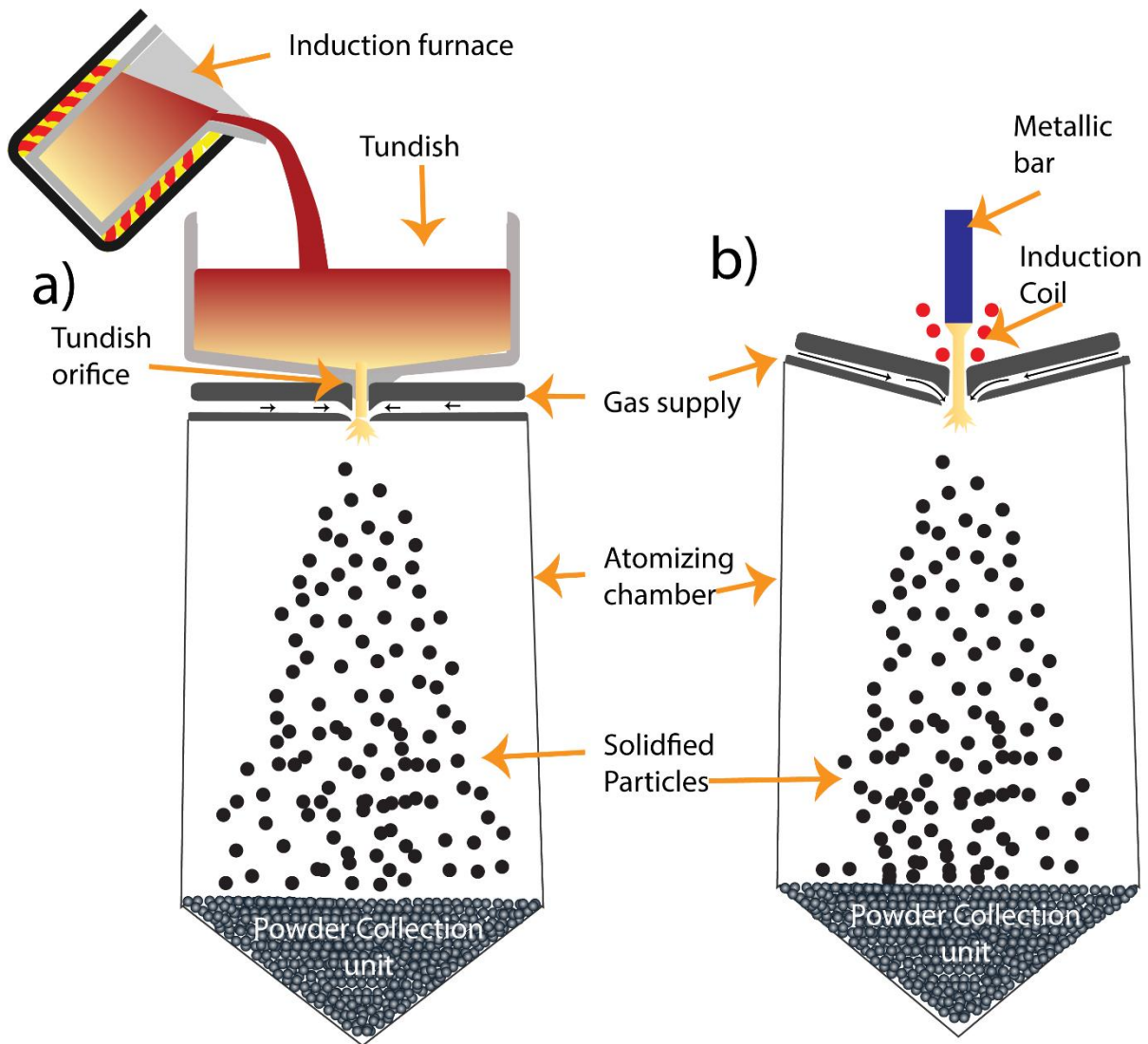


Figure 3: Gas atomization process in a schematic form where charging is happening through a) induction furnace, and b) electrode induction melting.

The micrographs in Figure 4 explain how the quality of powders produced using traditional gas atomization and EIGA of Alloy 718 differs. Gas atomization can provide a smaller particle size distribution due to regulated gas and melt flow, as shown in Figure 4a. However, turbulence in the melt flow can result in the creation of smaller particles that quickly solidify and settle as satellites on the surface of larger particles. In contrast, the design of the free-fall nozzle in EIGA allows gas jets to directly interact with the melt stream emanating from the electrode. Since there is a greater separation between the melt stream and the gas jet nozzle in this instance, part of the energy of the gas jets is lost before it interacts with the melt stream. As a consequence, the EIGA method produces coarser particle size. Despite this, the powder has almost no satellites, has a higher sphericity and cleaner surface (see Figure 4b), which is advantageous for its utilization in AM.

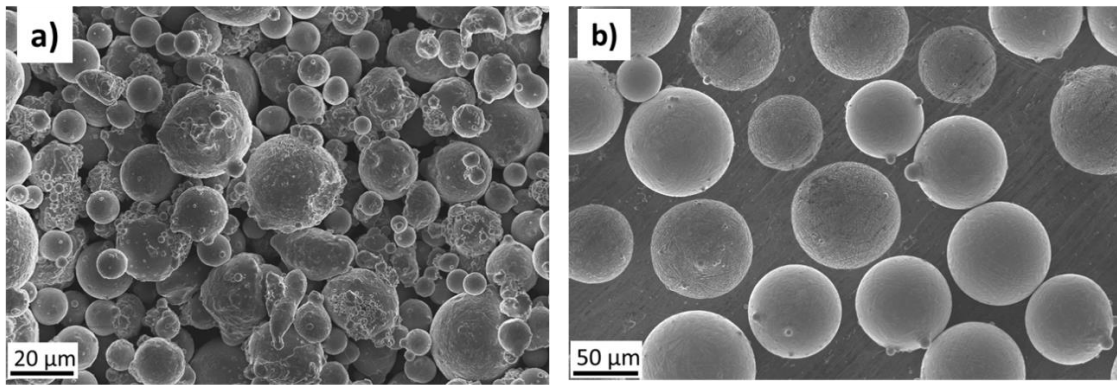


Figure 4: Comparison of Alloy 718 powders post sieving morphology produced by a) conventional gas atomization and b) electrode induction gas atomization.

3.4 Plasma atomization process

The plasma atomization method employs plasma torches as a heat and atomization source, as well as wire as a feedstock material [36], as shown in Figure 5. The plasma reacts with the wire, melting it and atomizing the melt. As in traditional gas atomization, the melted droplets solidify and aggregate. This method produces powder with high sphericity and a clean surface. However, there are several issues with this technique. The manufacturing rate is rather low, which raises the process cost. Because the feedstock material must be in the form of wire, it is not possible to modify the composition during atomization. The PSD of the powder produced using this method is between 0 and 150 microns, with a D50 of 40 μm . When high powder sphericity and purity are needed, which are challenging to handle by gas atomization, this process is mostly employed to make powders from Ti alloys as well as a variety of other sophisticated materials.

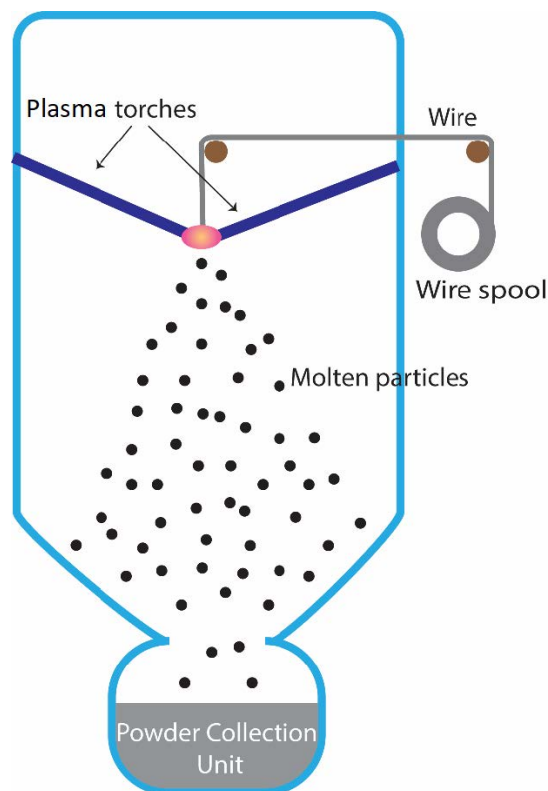


Figure 5: A schematic diagram of plasma arc melting with material charging through the wire.

3.5 Plasma rotating electrode process

High-grade metallic powder in terms of sphericity and surface cleanliness may be produced using the plasma rotating electrode technique [34]. Figure 6 illustrates this procedure, which involves physically rotating a metallic electrode while melting its end using a plasma torch. By use of centrifugal force, the liquid metal is propelled away and solidifies into a flawless sphere. Historically, coarse PSD was created using this approach. However, with the introduction of AM, new adjustments to the technique have been created where the acceleration of the electrode's rotation speed can help provide PSD that is appropriate for AM. The high-quality powder is created using this method for AM production of crucial components.

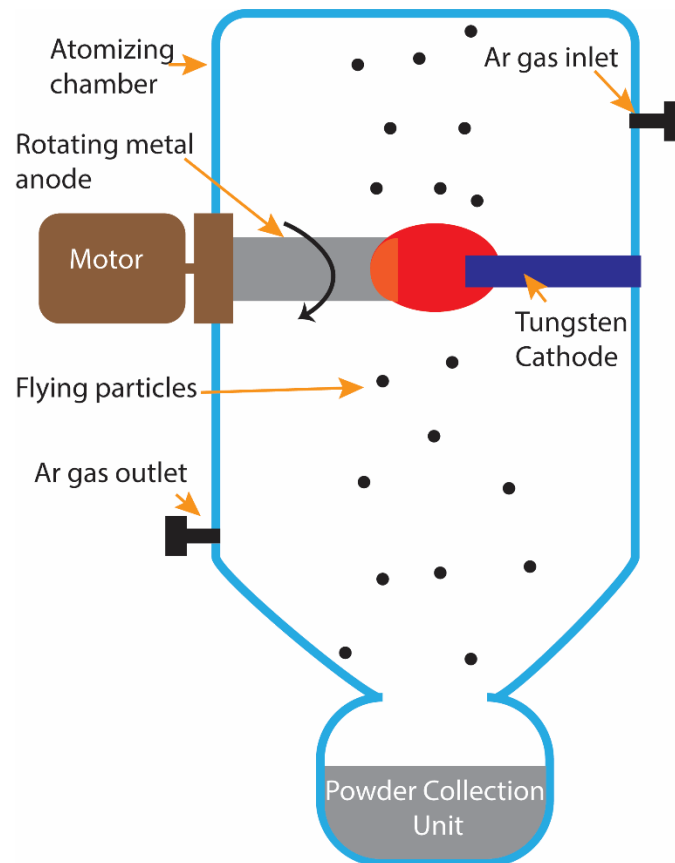


Figure 6: A schematic depiction of plasma rotating electrode with charging through rotating metal electrode.

3.6 Powder properties for additive manufacturing

Powder characteristics consideration is a crucial factor for the effective fabrication of AM products and is still a difficulty for researchers [37]. Both the interaction of powder with AM systems and the bulk qualities of the finished product are influenced by powder properties. In PBF processes, for instance, powder morphology can influence the density of the powder bed, surface roughness, melting/sintering kinetics, and density of the created component, among other things [38]. It is crucial to manage the powder's qualities to ensure repeatability and reproducibility. As a result, it is necessary to standardize the factors that must be considered before adding the powder to the machine. The key powder characteristics shown in Figure 7 should be evaluated to assess the powder's state. The following paragraphs briefly discuss these characteristics and their importance for AM.

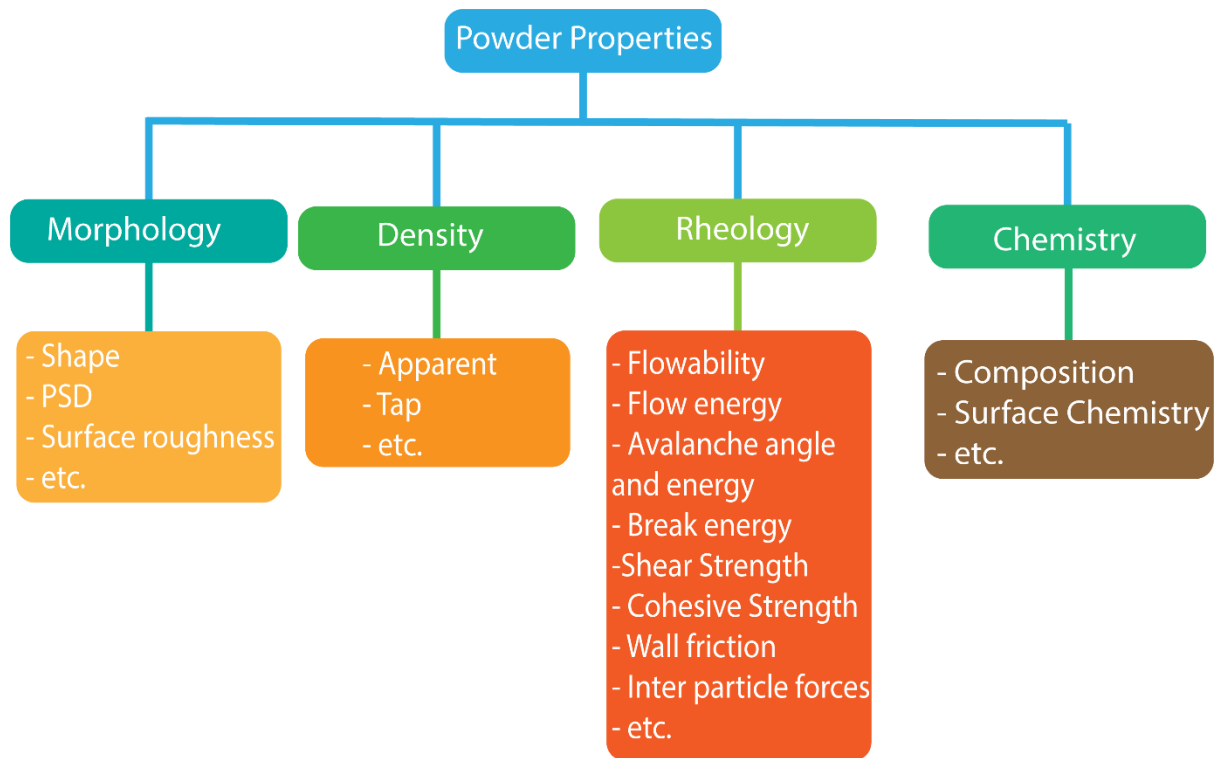


Figure 7: A tree diagram highlighting the important powder characteristics.

3.6.1 Morphology

The morphology of powder defined by shape, size, and surface roughness is a property of significance that determine the density and rheology of powder [39]. The shape of a particle can be described as spherical, dendritic, disc-shaped, angular, acicular, etc.[40]. Considering the requirement of better spreadability in AM, the sphericity and roundness of the particles have utmost importance. Sphericity purely determines the form of the particle and how close are all the cross-sections to the circle. It can be estimated by the ratio of smallest diameter to largest diameter. The closer the ratio is to the 1, the closer the shape of a particle is to a sphere. On the other hand, roundness is defined by the smoothness of the edges of particles. A particle with smoother shape of edges will have higher roundness. Figure 8 compares the AlSi10Mg powder produced through gas atomization with TiAl6V4 powder produced through plasma atomization. The difference among shapes is lucid where powder produced through plasma atomization has higher sphericity and roundedness compared to the powder fabricated by gas atomization.

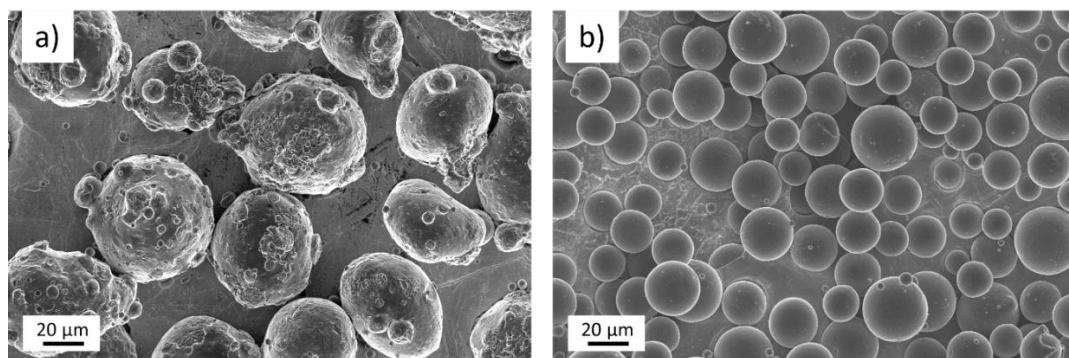


Figure 8: Comparison of surface morphology of a) AlSi10Mg produced through inert gas atomization and b) TiAl6V4 powder produced through plasma atomization.

Additionally, surface roughness is also a part of morphology which can strongly influence the rheological properties of AM powders. The adherence of satellite particles on the surface of the bigger particle can contribute towards the increase in surface roughness. During the reusage of spatters, a decrease in surface roughness by the detachment of satellite particles has been reported.

3.6.2 Powder size distribution

Powder size distribution (PSD) is also of particular interest when choosing the powders for AM as it determines the packing density, flowability, and compressibility of the powder [41]. Consideration of all three properties during the selection of PSD of powder for powder-based AM techniques is vital to achieve uniformity and to avoid pores, cracks, and inclusions. PSD can be measured by sieve analysis, laser diffraction, dynamic light diffraction, and image analysis. PSD is quantified by the apparent diameter measures of the powder mainly using D10 (the portion of particles with smaller than this diameter is 10%), D50 (the portion of particles with smaller than this diameter is 50%), and D90 (the portion of particles with smaller than this diameter is 90%). The size of AM feedstock powder is maintained by continuous sieving.

3.6.3 Density

The density of volume of powder is described using two measures: apparent density or tap density, which are different from the theoretical bulk density of the powder material. The apparent and tap density account for the gaps, voids and pores present in between the coinciding powder particles and depends upon how loosely/tightly the metal particles are packed to one another [42]. For powder bed techniques in AM, apparent and tap density are normally used as measure of the powder bed density. The high relative density of the powder bed is important to achieve higher part density. The spherical shape of the powder provides higher bed density and flowability, therefore, it is preferred over other shapes of powder. Along with shape, a smart choice of PSD range (with bimodal or trimodal particle sizes) can also play a significant role in achieving a higher density of powder bed where small particles can fit in the gaps between the large particles as shown in Figure 9.

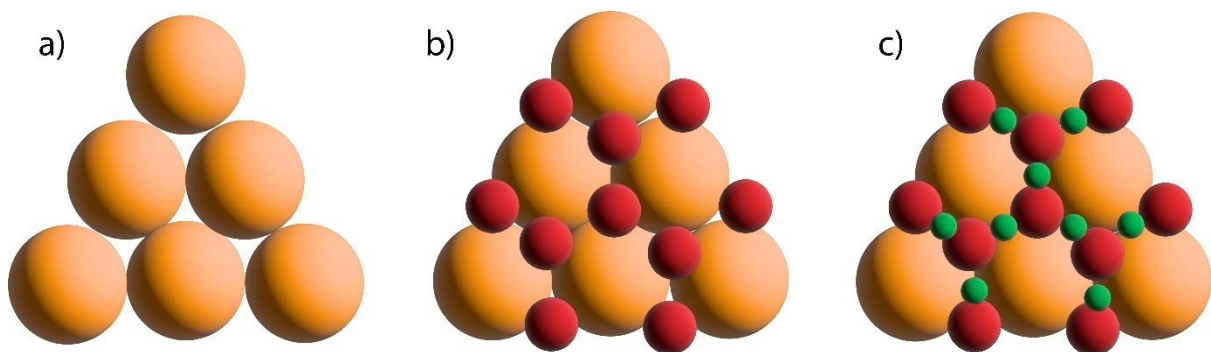


Figure 9: Effect of particle size distribution on packing where a) presents the uniform size which has large gaps in packing, b) presents a bimodal size distribution covering most of the gaps, and c) presents a trimodal size distribution covering all the visible gaps in between the powders.

3.6.4 Rheology

The need of spreading a fine powder layer with repeatability makes powder-based AM techniques sensitive to the variability in powder properties, particularly powder rheology [43]. Rheology in AM mainly deals with powder flowability, compressibility, flow energy, cohesion forces, inter-particle friction, wall friction, avalanche angle, etc. The rheology properties of the powder can be influenced by internal and external influences.

Internal influences mainly include particle size distribution, shape, surface roughness, density, and packing behavior. Whereas external influences consist of humidity, temperature, gas flow rate, raking method, etc. A range of techniques is used to measure various aspects of rheology including the Hall flowmeter funnel, carney funnel, Hausner ratio, circular cylinder analyzer, etc. [22]. Among all, the rotating drum analyzer is considered the most appropriate at the moment to predict the powder rheology closer to the standards of AM powder bed fusion techniques. In this technique, the powder is filled in a rotating drum where the flow characteristics of the powder are analyzed. A simple test can provide a range of powder rheology characteristics including powder flow, avalanche angle, break energy, dynamic density, packing, etc. at different speeds and temperatures.

3.6.5 Chemistry

Control of powder chemistry is critical to achieving reproducibility in the products manufactured through powder-based AM techniques. For AM powder, both bulk and surface chemistry require special consideration. The bulk chemistry is closely monitored during the atomization process. A small variation in the atomization process can include unwanted impurities and affect the overall chemistry of the powder. Sergi et al. compared the effect of the atomization route on the bulk chemistry of the powder and found that the oxygen, carbon, nitrogen, Al, and Si content can vary in alloy Inconel 625 greatly depending on the route of atomization [44]. A similar study by Riabov et al. showed that powder produced through CGA, EIGA, and water atomization (WA) has different oxide layer thickness and types of oxide on the surface of powder [35]. On the other hand, surface chemistry and the nature of oxide over the surface can influence the AM process greatly. For example, powder with a thick oxide layer will be hard to sinter in a powder cake during the PBF-EB process, and due to the lack of conducting path for electrons, there will be an accumulation of electrons on the powder bed. This can result in a small powder explosion on the powder bed, a phenomenon known as smoking. Moreover, the presence of an oxide layer can create defects in the fabricated part [45].

3.6.6 Variation in powder properties with reusability

While chemistry and microstructural qualities are concerned with the metallurgical quality of the powder, the rheology, density, and morphology are process-related elements of powder that help forecast the processability of powder in additive manufacturing. Most of the current research on powder characteristics is concentrated on the morphology and rheology of the substance. Reusability-related powder quality is frequently assessed by comparing PSD and flowability variations [46]. The TiAl6V4, Alloy 718, AlSi10Mg, and Scalmalloy powders were thoroughly analyzed by Cordova et al. [46] to ascertain the impact of powder reusability on PSD and flowability. The findings revealed a modest rise in PSD, especially for Alloy 718 and AlSi10Mg, which may be reduced by properly applying screening after each build. Additionally, the results demonstrated that due to the loss of tiny particles in reuse, the flowability of reused powder was superior to that of fresh powder. Because of the strong affinity of Al for oxidation, the bulk chemical analysis also revealed an increase in the oxygen concentration for the alloy AlSi10Mg. After reusability assessment, this is the analysis's lone negative finding. Concerning PSD, flowability, and oxygen pickup after using AISI 304 L alloy powder for 7 construction cycles, Sutton et al. [24] also reported comparable results. As a result, rheology (which improves for reused powder) and PSD (which may be adjusted by the screening process) can only aid in assessing the processability of powder in a PBF machine, not the quality of powder

and how it affects the attributes of manufactured components. As a result, process development is required to analyze the quality aspect of powder during reusability, which may be accomplished by specialized chemical analysis.

There are two types of chemical analysis: bulk composition and surface chemistry. Bulk composition analysis is a quick approach to determine the composition change from virgin to reused powder while considering the particle's surface and bulk chemistry. This information, however, must be supplemented by a complete surface chemical analysis to determine the distribution of oxygen on the powder surface, the primary oxide-producing components, and the change in oxide layer thickness. It is essential to comprehend the kind of oxide and the thickness of the oxide layer to predict how the oxide will behave in melt pools and during laser-powder interactions (i.e., whether it will dissolve, mix or float). Identifying the major oxide-forming components in each alloy can also reveal the depletion of important elements in bulk (e.g., Al in Alloy 718).

4 Powder degradation in PBF processes

Powder degradation in PBF processes mainly includes the oxidation of powder, agglomeration, change in powder size distribution, etc. The latter aspects of powder degradation can be controlled by the sieving of powder where agglomerates can be removed and the PSD can be adjusted. However, powder oxidation is a permanent expectation of degradation which cannot be removed like others. This chapter of the thesis is focused on the oxidation of metallic powders and how it varies for different AM techniques.

4.1 Oxidation of metals

Metallic elements are more stable in their oxide state compared to the metallic state at ambient conditions, except for gold. Oxidation involves a reaction between metals and oxygen and oxygen-containing species at a higher temperature where no aqueous media is involved. The rate of oxidation is dictated by the type of oxide layer formation. Mainly three types of oxide layers exist for metals: unstable, volatile/molten and stable. In the case of the unstable oxide layer, the metal surface does not get tarnished by the oxide layer e.g. gold. An example of a volatile/molten oxide layer is V_2O_5 which means that the vanadium is continuously degraded upon oxidation at elevated temperatures. Another example of the unstable oxide layer at high temperatures is that on Ti metal where oxygen from the oxide layer gets dissolved into the matrix as Ti has a very high solid solubility for atomic oxygen. A commonly found type is the thin stable oxide layer which once formed hinders further oxidation e.g. Cr, Al, etc, owing to its slow growth kinetics.

4.1.1 Thermodynamics of oxidation

This part covers the fundamentals of thermodynamics, which aids in understand the favored stability of distinct oxides. The fact that most of these estimates are for equilibrium conditions, which are vastly different from the actual conditions during oxide formation on powder exposed to the AM environment, this is a critical aspect (especially during oxidation of spatter particles). The thermodynamics of oxidation do, however, help us to understand the likelihood of specific oxides forming in complicated mixtures. The main idea underlying the driving force calculations is the change in free energy (G) for the reaction from metal to oxide state, which can be calculated using the following equation:

$$\Delta G = \Delta H - T\Delta S \quad (1)$$

Here, ΔH represents the enthalpy change, ΔS represents the entropy change, and T represents the temperature in Kelvin degrees. Due to the exothermic nature of oxidation, the ΔG has a negative value. In such a case, the desired oxidation of components in complex alloys is a major factor. For example, in a simple alloy like AlSi10Mg, all three primary alloying elements have high oxidation susceptibility, but Al and Mg have preferred oxidation compared to Si in the sense that the stronger oxide forming would react with oxygen first if there is no kinetic restriction.

The Ellingham diagram, which is a collection of typical free energy changes, is also shown in Figure 10 where the temperature (T) dependence of ΔG^0 for the development of oxides from their constituent elements is presented. The standard free energy change can be described by the following equation at equilibrium at which $G=0$:

$$\Delta G^0 = -RT\ln(K) \quad (2)$$

The equilibrium constant in this case is K , while the gas constant is R . This equation may be written as follows for oxidation/reduction processes, considering the pure metals and the corresponding oxide formation:

$$\Delta G^0 = -RT \ln(pO_2) \quad (3)$$

With an increase in temperature and partial pressures of different gases, such as pO_2 , pH_2/pH_2O , and pCO/pCO_2 , the Ellingham diagram is particularly helpful in determining the oxide stability. The latter two equilibrium ratios are simply generated from the oxidation of H_2 to H_2O and CO to CO_2 . The bottom of the Figure 10 shows the reactive metals, which are prone to oxidation, while the top shows metals with lower oxide stability, which are easier to reduce. According to the diagram, it might be expected that the elements at the bottom (such as Al , Ti , and Cr) would oxidize more quickly than Fe , but this does not happen because these metals develop a thin protective oxide layer on their surfaces, shielding the metal from oxygen and preventing further oxidation. Additionally, when the temperature rises, oxide loses stability and the ΔG^0 value lowers. This results from the reaction's accompanying reduced entropy.

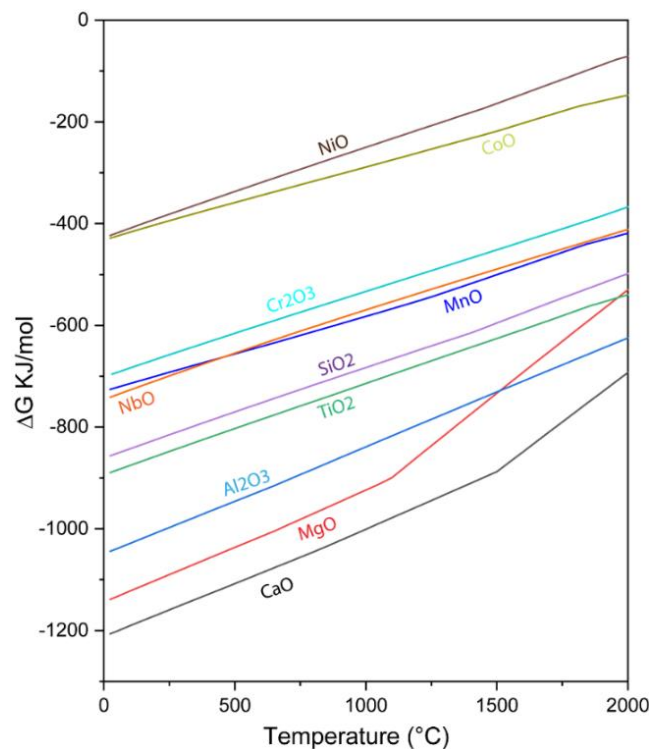


Figure 10: An Ellingham diagram highlighting the change in Gibbs free energy for oxide formation with temperature. The graph is plotted using HSC9.0 software.

4.2 Powder degradation in PBF-LB

Surface oxidation and spatter generation are the two primary mechanisms that might potentially contribute to the deterioration of unconsumed powder in the powder bed in laser powder bed fusion.

4.2.1 Feedstock powder oxidation by atmospheric exposure

Due to the high surface-to-volume ratio, powder surface oxidation is a well-known phenomenon in the field of powder technology. Surface oxidation is particularly prominent for alloys made of highly oxidation-prone elements including Al , Cr , Ti , and Zr [47,48]. However, the formation of a homogeneous oxide layer on the surface of such alloy powders, passivates

and prevents it from further oxidation unless any external parameters such as temperature, humidity, chemical treatment, etc. influences the passive layer. Here, a positive aspect of the PBF-LB process is that the powder bed is placed in an inert environment and close to ambient temperatures during the process. These conditions ultimately assist in restricting the further oxidation of the powder.

After 31 reuse cycles (about 600 hours of machine time), Quintana et al. during investigation on the reusability of TiAl6V4 powder revealed a meager 30% increase in oxygen concentration [25]. This stability resulted from the stable TiO₂ layer development, which stopped the powder from further oxidizing. Furthermore, a study by Skalon et al. [49] on TiAl6V4 powder reuse showed that powder degradation influenced the melt stability, melt flow, formation of lack fusion defects, and mechanical properties. However, an in-depth analysis of reused powder showed that the degradation was mainly influenced by the accumulation of spatters which are discussed in following section. Another study on Alloy 718 by Ardila et al. [50] showed no discernible difference in the chemistry between recycled powder and fresh powder. Based on these findings, it can be said that the predominant powder degradation mechanism in the PBF-LB process is not the oxidation of feedstock powder by atmospheric exposure. It is rather connected to spatter accumulation in the powder which is discussed in the following section.

4.2.2 Spatter formation and accumulation in reused powder

A dominant powder degrading mechanism in the PBF-LB process could be the generation and buildup of spatter in the powder bed [51]. By-products of the PBF-LB process, which are generated by the interaction of a laser-powder-melt, are termed spatters. Spatters produced by laser-powder-melt interactions can differ in size, shape, morphology, and chemistry on an individual basis [52–55]. These deviations are connected to the spatter particle formation mechanism. Figure 11 depicts a schematic of the PBF-LB process and highlights the typical particles produced by the laser-melt-powder interaction. The difference in temperature and origin of the spatter particles is represented by the colour of the ejecting spatter particles. First, the molten material that is ejected from the melt pool because of recoil pressure is known as the melt pool ejecta [56]. Here, recoil pressure is the pressure on the surface of the melt pool which occurs by the expansion of vapors during laser-powder interaction and vaporization [57]. This molten ejection has two possible outcomes: it can either solidify in flight and rest on a bed of powder, or it can combine with other ejecting particles to produce larger particles [58]. But if this ejected melt touches a powder bed before solidifying, it can come together with the pre-existing powder to create agglomerates. Second, low-pressure zones or the collision of metallic vapors can propel spatters from the powder bed [57]. These spatters are referred to as entrained particles. Depending upon the possibility of interaction of these particles with the laser beam, the entrained particles can be cold or hot [20]. The cold spatters are usually unaffected spatter particles with a virgin-like clean surface. Contrarily to cold spatters, some entrained particles might interact with the laser during ejection and appear as hot particles. Such hot particles are frequently partly molten or have temperatures that are close to melting [59]. Hence, hot particles are highly susceptible to surface oxide by picking up the oxygen present in the build chamber.

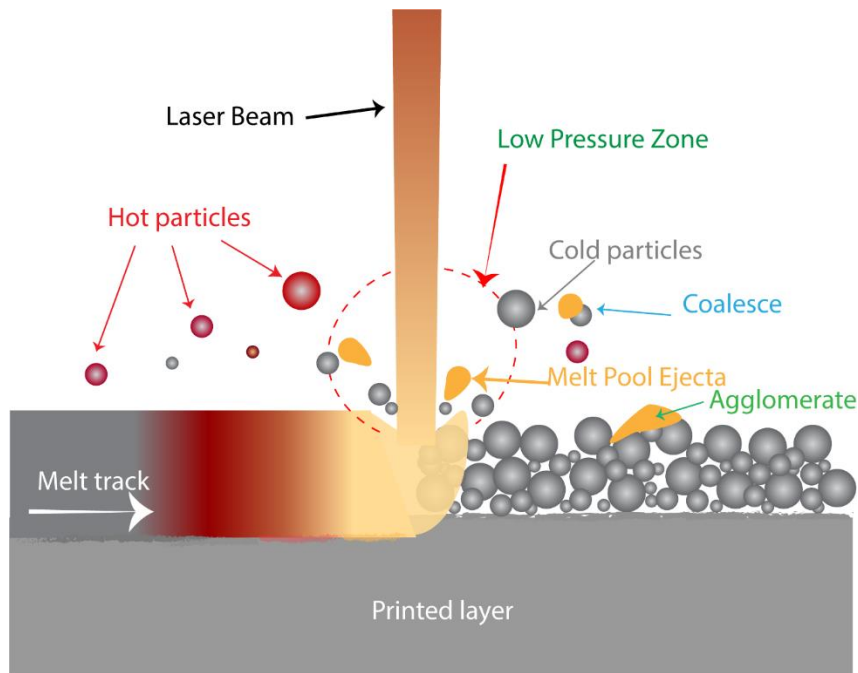


Figure 11: A schematic showing spatters formation in the PBF-LB process.

The amount of energy in the beam, the size of the beam, the speed of the scan, the material, the purity of the processing gas, and many other variables may all influence the formation of spatters. Gunenthiram et al. [60] evaluated the rate of spatter formation in 316L and AlSi10Mg alloy and found that 316L stainless steel created larger number of spatters compared to Al12Si alloy in their study on the connection of materials' effects on spatter generation. The low upward trajectory of Al12Si spatters, which aided in the assimilation of ejected particles in the melt pool, was cited as the cause. There still existed a lack of understanding regarding the evaluation of the effect of part geometry and atmospheric gas on the generation of spatters which has been assessed in this thesis.

Spatter generation can have a variety of effects on the build quality. First, when the laser beam interacts with the spatters during the time of flight, the laser beam is attenuated, which causes a discontinuity in the energy input to the build layer and may lead to a defect [51]. Second, by altering the layer thickness of the powder bed, the redeposition of spatters on the powder bed might adversely affect the component properties. Thirdly, the buildup of these particles can have a detrimental impact on the PSD, morphology, and flowability of powder, which can affect the qualities of components that have been manufactured [61]. Finally, in hot spatters, mass transfer of elements with strong oxygen affinity can take place. Such particles have the potential to oxidize, and their buildup in a powder bed may raise the powder bed's total oxygen concentration. This may cause the development of oxide inclusions in the manufactured component and local discontinuities in the absorption of energy (change in energy coupling between energy source and powder) [62]. Additionally, the oxidation behavior of spatter particles might differ from one material to another, making it crucial to study this behavior using a specialized surface analysis.

4.3 Powder degradation in the PBF-EB process

The PBF-EB process runs at a high temperature (650-1050 °C). These temperatures are relatively high and so allow for rather intensive mass-transfer of elements with a strong affinity

for oxygen from the particle's center to the surface of the powder more swiftly. Numerous studies have published their findings about oxygen pickup during TiAl6V4 and Alloy 718 PBF-EB processing [63,64]. TiAl6V4 powder that had been gas atomized was examined in research by Nandwana et al. [65]. The analysis revealed a linear rise in oxygen concentration across five cycles, from 0.14 weight percent to 0.18 weight percent. In a related study on TiAl6V4, Ghods et al. [63], similarly demonstrated a linear rise in grade 5 TiAl6V4's oxygen content from 0.14 weight percent in virgin to 0.20 weight percent after 11 cycles. However, Shanbhag et al. [66] saw a quick rise in grade 5 TiAl6V4 powder from 0.13 weight percent to 0.17 weight percent in just two cycles. Nandwana et al. [67] also noted a rise in oxygen content for Alloy 718, going from 0.014 weight percent to 0.022 weight percent after 6 cycles. Gruber et al. [14] noted a rise in oxygen level for the same alloy after 14 reuse cycles, going from 0.0146 weight percent to 0.0266 weight percent. These results lead to the conclusion that, because of the exceptionally high process temperature, powder oxidation is the predominant degrading mechanism in the PBF-EB process. However, the referenced studies on the rate of oxidation for both TiAl6V4 and Alloy 718 show an inconsistency regarding the rate of oxygen pickup.

These discrepancies may be related to the differences in process conditions during PBF-EB processing and the environment of powder handling. The humidity in the air used for handling powder can also affect oxygen availability during the build. According to Nandwana et al. [65], water adsorbed on the surface of the powder is the primary cause of oxygen contamination in the PBF-EB chamber. Such adsorption occurs when the powder is exposed to air (during sieving and storage). Processing in a humid atmosphere can increase the quantity of water that is adsorbed on the powder surface, which increases the rate at which oxygen is picked up, and vice versa. Additionally, handling powder in an environment of air might result in the creation of Ni and Fe-based oxides and hydroxides [14]. These oxides are unstable at high temperatures and can shift oxygen to elements that produce stable oxides, increasing the proportion of stable oxides [14]. Therefore, the PBF-EB process' inconsistent rate of powder oxidation may be attributed to the combination of all its process variables.

Additionally, the type of oxides and the tendency for oxidation might vary amongst alloys. Gruber et al. [14] examined the surface behavior of powder while recycling it for 30 build iterations in a study on Alloy 718. The results demonstrated that the oxide growth on the surface of the powder is not homogeneous. Instead, it takes the shape of oxide particulates dominantly containing aluminum. As the number of reusability cycles grew, so did the volume and coarseness of these oxides. According to the Ellingham diagram in Figure 10, the most negative standard Gibbs free energy change is for Al forming Al_2O_3 in comparison to the formation of Ti, Cr, Fe, and Ni oxides, showing the formation and stability of Al-based oxides. Furthermore, Al_2O_3 is more stable at the PBF-EB conditions and the oxidation of Al means that this element can act as a getter and lead to the reduction of the oxides of other elements (see Figure 12). Figure 12 illustrates how the presence of any Ni or Fe-based oxides, or hydroxides means that oxygen can be redistributed and react with more stable oxide-forming elements like Al, Ti, Cr, etc.

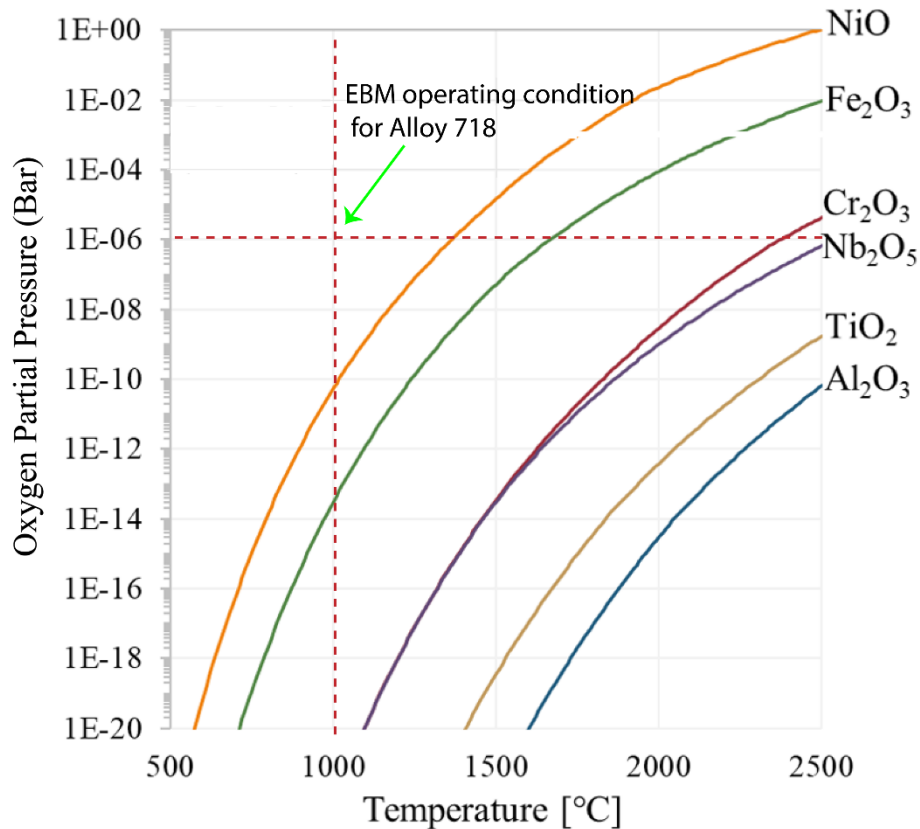


Figure 12: Equilibrium oxygen partial pressure for some elements of Alloy 718 in the oxide form.

On the other hand, Sun et al. showed that the processing of TiAl4V6 in the PBF-EB demonstrated the development of a homogeneous oxide layer over the surface [68]. They discovered that even after 30 iterations of the cycle and a 35% rise in the typical powder oxygen concentration, the oxide layer's thickness remained below 10 nm. While the pickup of oxygen resulted in the enrichment of oxygen in the β phase. A continual increase in oxygen concentration without a noticeably different oxide layer thickness was also demonstrated by Montelione et al. [64]. As a result, the ability to pick up oxygen differs depending on the alloy's composition, thus it's critical to identify the variables causing rapid oxidation and study the oxidation behavior of powder. It should be noted that Ti has a high solubility for oxygen in its alpha phase, making it capable of acting as oxygen-getter material in vacuum conditions.

4.3.1 Sublimation of metallic elements during PBF-EB

Due to the PBF-EB methods' primary needs of a high vacuum and high temperature, these circumstances might hasten the sublimation of materials containing elements with higher vapor pressure, such as Al and Cr [69]. Sublimation of aluminum is noticeable and frequently seen, especially for alloys like TiAl and TiAl6V4. Previous work on TiAl found that the amount of Al decreased from the virgin powder to the manufactured components by up to 7.0% [70]. Another work on TiAl6V4 by Petrovic et al. [71] found that after 12 reuse cycles, the Al concentration had decreased by 3%. As a result, sublimation is also a crucial factor in the PBF-EB process. A few recent studies have focused on process improvement to lower the rate of sublimation from the melt pool. The change in a built sample Al-loss from the virgin powder was reduced to only 1.5 at. % thanks to research by Schwerdtfeger et al. [29] on the optimization of layer thickness and total volumetric energy density during processing Alloy 718. In separate research, Damri et al. [72] proposed raising the built-chamber pressure by one

order of magnitude (from 10^{-3} mbar to 10^{-2} mbar), which did not affect the energy effectiveness of the beam but it could lessen minimize evaporation.

5 Materials

5.1 Aluminum alloys

Aluminum and its alloys provide a great combination of properties to make them very versatile materials to be used in a range of applications. This is the reason why the consumption of Al-based materials in structural applications is the second largest after steel [73]. High-strength Al alloys are preferred over structural steel due to the high strength-to-weight ratio, particularly for the moving parts in e.g., automobile, and aerospace industries. The ease of fabrication of Al alloys into any shape is an important asset and can help it to compete with cheaper materials with low workability.

Conventionally, Al alloys are divided into two main categories which include: wrought alloys and cast alloys. The wrought alloys usually contain smaller alloying elements concentration which lies between 1-2 %. Whereas the cast alloys contain around 10-12 % concentration of alloying elements. A further division can be made depending upon the ability to heat treat. The first category is heat-treatable alloys, where the strength of an alloy can be managed by solution treatment, quenching and age hardening using appropriate heat treatment. In both alloy types (wrought and cast), such alloys are called heat-treatable alloys. The other subclass of alloys relies specifically on work hardening and mechanical reduction for property development and are termed work hardening alloys.

For the identification of alloys both in the wrought and cast category, a nomenclature system is developed [74]. The wrought alloys are divided on a four-digit system from 1xxx to 9xxx depending upon the constituents and properties. Among those, 2xxx (Al-Cu, Al-Cu-Mg), 6xxx (Al-Si-Mg), and 7xxx (Al-Zn-Mg) are heat-treatable alloys and can be strengthened by precipitation hardening. Moreover, 1xxx, 3xxx, 4xxx, and 5xxx are non-heat treatable alloys. The cast alloys are identified by a three-digit system followed by a decimal and again divided from 1xx.x to 9xx.x. In cast alloys, 2xx.x (Al-Cu), 3xx.x (Al-Si), and 7xx.x (Al-Zn) are heat-treatable alloys [74].

5.1.1 Additive Manufacturing of Aluminum alloys

Among PBF processes, PBF-LB is the more widely used process for Aluminum alloys [75]. Yet, the number of printable Al alloys through PBF-LB is still very low and several factors are the resisting factors in the processability of these alloys. Such factors include the high thermal conductivity of Al, low laser absorption at commonly used laser wavelengths, low flowability of the melt pool, and surface oxide formation on powders.

The high-strength wrought alloys, e.g. 2xxx, 6xxx, and 7xxx series, are commonly used Al alloy systems for the aerospace and automobile industries [76]. However, many researchers reported that cracking/hot-cracking during the processing of these alloys make them difficult candidates to process through the PBF-LB process. The cracking phenomenon in these alloys is driven by the large volume fraction of high-angle grain boundaries, enrichment of solute atoms on grain boundaries by cyclic solidification and re-melting, and solid-state diffusion of solute atoms to the grain boundary. Such grain boundary segregation results in hot cracking. Furthermore, the cracking in these alloys can be attributed to the difference between solidus and liquidus temperatures, the poor flowability of melt, and the coefficient of thermal expansion. There are a few wrought Al alloy systems that are specifically developed for AM use, such as an alloy designed by Aeromet based on 2xxx with the addition of Ti, A2XTM (Al-4.5Cu-0.3Mg-0.7Ag-3.5Ti), the Airbus alloy based on 5xxx with the addition of Zr and Sc

known as Scalmetalloy® (Al-4.5Mg-0.6Sc-0.5Mn-0.3 Zr), and the HRL laboratory one based on 7xxx with the addition of Zr, Al-7A77 alloy (Al-5.5Zn-1.5Cu-2.5Mg-1.5Zr) [76].

Weldable cast alloys with near eutectic composition are the most widely adapted Al alloy systems in AM, e.g. AlSi10 [77]. The AlSi10 is a near eutectic alloy that has excellent thermal conductivity, high flowability, and low thermal expansion coefficient which makes it an ideal candidate for the PBF-LB process. However, this system has lower strength which can be relatively improved by the addition of Mg (<1 at. %) which forms Mg₂Si precipitation to improve the strength of the alloy [78]. Consequently, the main alloy is AlSi10Mg. Considering the high reactivity of Al and Mg elements and susceptibility for oxidation, investigation of the feedstock powder of this alloy is important.

5.2 Nickel-based superalloys

High temperature and corrosive environments in aerospace engines, energy turbines, nuclear power plants and chemical and petrochemical applications require materials with excellent mechanical properties, particularly strength, toughness, creep and fatigue properties, and high oxidation/corrosion resistance [79]. Nickel-based superalloys are known to have exceptional high-temperature properties and can be used in a variety of critical applications. The superior properties of Ni-based superalloys originate from the γ' coherent precipitate phase formation with the basic composition of Ni₃(Al, Ti) in γ phase where both phases have a face-centered cubic structure [80]. By variation in the volume fraction of γ' and additional carbide formation by various elements, multiple types of superalloys can be customized depending upon the properties required in the aimed application.

5.2.1 Additive manufacturing of superalloys

Although the volume fraction of γ' is critical to reaping the full benefit of Ni-based superalloys, the γ' volume fraction impact negatively on the weldability of the superalloys. Ti and Al are two main γ' phase-forming elements. An increase in the concentration of these elements negatively affects the weldability of the Ni-based superalloys [81,82]. Superalloys with lower content of Al and Ti, such as Alloy 718, Hastelloy X, Alloy 625, and C263, are the superalloys with reasonable weldability for being used for processing in AM techniques [83]. The processing of non-weldable superalloys so far results in cracking in the fabricated parts.

The Ni-based superalloys are mostly processed by PBF-LB and PBF-EB processes. A review by Sanchez et al. [83] revealed that 86 % of the published research on the processing of Ni-based superalloys is connected to weldable alloys where Alloy 718 was leading at 68% followed by Alloy 625 at 18 % and Hastelloy X at 3 %. Considering the low concentration of Al and Ti in these alloys, the critical role of these elements to obtain good properties, and their susceptibility to oxidation makes it essential to evaluate the oxidation/degradation of feedstock powder during the processing of the alloys in PBF techniques.

5.3 Titanium alloys

Titanium is a metal with exceptional mechanical strength, corrosion/oxidation resistance, formability, weldability and low density [84]. The Ti alloys are mostly used in high-end products in the aerospace, medical, industry, etc., as the production of metallic Ti is quite expensive (approximately 15 times more expensive than that of Al). Pure Ti without any addition of alloying elements has exceptional properties and is widely used in the medical industry for bio-implants. However, alloying elements can enhance their properties by introducing a secondary phase. At room temperature, Ti possesses a hexagonal closed pack

(HCP) structure which is also referred to as α phase. At 890 °C, an allotropic transition occurs in Ti where the crystal structure transforms from α (HCP) to β (BCC) structure which remains stable to the melting point. Some alloying elements reduce the transition temperature from α to β phase and are called β stabilizers like vanadium, molybdenum, niobium, tantalum, iron, manganese, cobalt, nickel, copper, and silicon. Some α stabilizers raise the transition temperature as aluminum, gallium, carbon, oxygen, germanium, nitrogen, etc. The properties of α and β phases are quite different where the β phase is relatively ductile due to the higher number of slip planes in the BCC structure. On the other hand, the α phase possesses higher strength and lower ductility due to the HCP crystal structure. The most used Ti alloy is TiAl6V4 which contains the combination of both α and β phase and has a high specific strength and excellent corrosion resistance. It is extensively used in medical implants, aerospace, gas turbines, the chemical industry, etc. The properties of TiAl6V4 are decisively dependent on the microstructure.

5.3.1 Additive manufacturing of Ti Alloys

Titanium alloys have poor machinability and fabricating complex designs of Ti alloys is very expensive. Hence, AM provides a unique opportunity to fabricate Ti parts with complex geometries [85]. Currently, Ti alloys are mostly processed through powder bed fusion (PBF) processes. The major concern regarding the processing of Ti alloys with AM technologies has been impurity control where oxidation, hydrogenation, and nitration of the feedstock/product can deteriorate the properties substantially [86]. However, the advancement in AM technology enables it to control the level of impurities now where the oxygen contamination level can be maintained at <0.2 wt%. Currently, commercially pure Ti (CP Ti) and TiAl6V4 alloys are most fabricated variants by means of additive manufacturing processes due to their wide scale of applications.

6 Experimental Methods

The experimental plan for sample collection and the employed characterization techniques have been discussed in this chapter.

6.1 Materials and processing

The studies presented in this thesis include the work on PBF-LB and PBF-EB where AlSi10Mg, Alloy718, Hastelloy X, and TiAl6V4 are processed by the PBF-LB and Alloy 718 processed by the PBF-EB. This section discusses the alloy composition, processing strategy, and sample collection.

6.1.1 PBF-LB processing of AlSi10Mg

AlSi10Mg alloy powder was provided from Concept Laser GmbH with nominal compositions of Si 10.1 wt.%, Mg 0.4 wt.%, and Fe 0.11 wt.% balanced with Al. The range of the virgin particle size distribution was D10= 45 μm , D50= 65 μm , and D90= 93 μm . The powder was manufactured via gas (nitrogen) atomization, and as a result, it is approximately spherical in shape with satellites adhering to its surface. The satellites are small, 5 μm -diameter particles that form during atomization and stick to the surface of bigger particles.

The build chamber dimension of the XLINE 2000R Concept Laser GmbH machine is 800x400x500 mm³. To maintain the same regulated inert environment while reusing the powder, the machine incorporates an integrated-sieving station and silo system that is linked to the build chamber [44]. Fresh nitrogen gas is fed into the build area and sieve station to keep an oxygen level below 1000 ppm. Except for the moment the build chamber is opened to remove the build plate at the end of the build process, the powder stays in the inert environment. The unconsumed powder is briefly exposed to the outside air while the build plate is removed. In the glove box, the leftover powder from the printing plate is removed under an inert environment. The powder is delivered from the glove box to the sieve station through the piping. To improve the repeatability of the product's qualities, the sieving station sieves the powder to retain the virgin powder-like particle size distribution.

At any one time, the system uses around 550 kg of AlSi10Mg powder. To make up for the powder lost during the production process, some virgin powder top-up is done. In conclusion, both new and used powder is included in the powder combination that was utilized for the experiment. The reused powder under study in this work is a residue of the PBF-LB machine's continuous operation for 30 months, with a system uptime of around 2000 hours annually. Five total samples were gathered over the course of 30 months to investigate the change in powder quality and, therefore, the rate of deterioration. The period and annotation for each sample utilized in this analysis are shown in Table 3.

Table 3: The annotation for the samples where numbers are representing the number of reused months

Sample name	Time in machine
A10	Virgin powder
A16	6 months
A110	10 months
A114	14 months
A130	30 months

6.1.2 PBF-LB Processing of Alloy 718

For all the studies included in the thesis, the used Alloy 718 powder was produced through gas atomization and the particle size distribution lay in the range of 15 μm to 45 μm . The supplier of the powder was Höganäs AB, Sweden. The analysis of particle size distribution (PSD) was done by laser diffraction using Mastersizer 3000 (Malvern Panalytical) equipment. The outcomes of five measurements resulted in the following average data: $D_{10} = 17.8 \pm 0.1 \mu\text{m}$, $D_{50} = 30.1 \pm 0.1 \mu\text{m}$, and $D_{90} = 49.5 \pm 0.2 \mu\text{m}$.

Table 4: Measured composition of Alloy 718 powder used in experimentation

Element	wt. %	Element	wt. %
Ni	53.95	Co	0.01
Cr	18.28	Mn	0.02
Fe	Bal.	B	0.001
Nb	5.12	Si	0.03
Mo	3.04	Cu	0.04
Ti	1.02	N	90
Al	0.5	O	150
C	0.05	P	<0.01
Ta	<0.01	S	<0.005

Three publications based on the PBF-LB processing of Alloy 718 are part of this thesis (Papers ...). The equipment and processing parameters used in the provided research share certain similarities, although the build and sampling methods varied from one study to the next. The similarities are mainly connected to the machine and some laser parameters. The EOS M290 (EOS GmbH) L-PBF machine was utilized to carry out all the investigations. A 400 W nominal power Yb-fiber laser is included in this setup. With a 40 μm layer thickness, the Alloy 718 standard EOS parameters were used (license name: ALLOY 718 PerformanceM291 2.11).

High-quality argon (Argon 4.6) was utilized at normal working conditions for sample collection presented in Paper III. The purpose of the capsules was to encapsulate powder during the PBF-LB process to study the spatter formation and accumulation in the powder bed. The lattices were introduced to evaluate the effect of part geometry and overhang structures on the generation of the spatters. The containers are named after the length and diameter of the lattice beams, for example, L7D3 (length = 7 mm and diameter = 3 mm), and containers are self-supporting by design. Although the diameter and length of the lattice beams varied, they had the same lattice structure, as illustrated in Figure 13. Three lattice-structure-filled containers labeled as Empty, L7D1, L7D3, and L3D1 were positioned near the gas inlet on the build platform, which is where new shielding gas enters to cover the process area. To make removal simple after the building process was complete, the capsules were constructed on top of a support framework that was 2 mm thick. The capsule caps were made with a thin connection to the body of the container, allowing the powder samples to be removed for examination by breaking the connection. Chemical and surface analytical methods were used to examine the powder that was enclosed in containers.

Optical tomography (EOSTATE Exposure OT, provided by EOS GmbH) was used in this work as an extra component to describe the creation of online spatters. Details on the optical tomography performed by Dr. Zhuoer Chen may be found in Paper III.

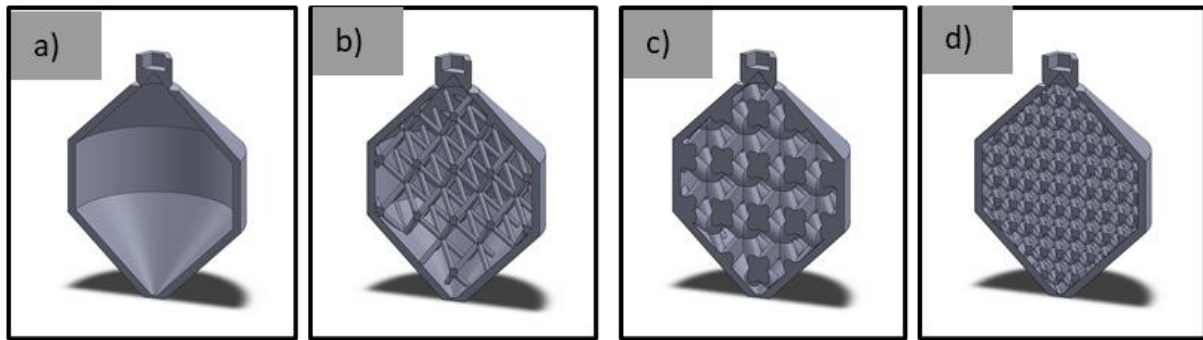


Figure 13: The designed containers with the changing parameters with a) empty, b) L7D1, c) L7D3, and d) L3D1 containers. Here, the L in the naming denotes to the distance between two parallel lattices and joints and d indicates the diameter of the lattice bars in mm (Containers designed by M. Fischer and Z. Chen in CAM² center).

The result presented in Paper IV is based on a study done on Alloy 718 where the powder was processed in a high-quality argon environment (Argon 4.6) and the oxygen level was maintained below 1000 ppm. In this investigation, four large cylinders with a few capsules were built using a 21-hour-long build job. To further understand the oxidation behavior of Alloy 718 spatters, the spatter particles deposited on the gas intake and outflow were carefully collected and examined.

Paper V is based on the effect of residual oxygen content on the oxidation of spatters from alloy 718. As the process gas, high-purity technical Ar (Argon 5.0 with a maximum of 10 ppm oxygen) was employed. The ADDvance®O₂ precise external oxygen monitoring device was linked to the PBF-LB machine (Linde GmbH). The holding gas flow for the machine, which is generally present to limit leaks, was manually turned off during the use of the ADDvance®O₂ precision (Linde GmbH) system to stabilize the residual oxygen level. Using this method, the high-purity gas flow within the recirculation system could be adjusted, allowing control of the remaining oxygen in the chamber. It makes use of an electrochemical cell to test and regulate purity. In that study, the system was employed to repeat the same printing cycle while maintaining a regulated oxygen content in the build chamber, with an accuracy of 10 ppm determined by an electrochemical cell, to a minimum level of 20 ppm as well as 400, 600, 800, and 1,000 ppm of residual oxygen. Typically, during PBF-LB processing, spatters move against the gas flow deposit on the gas input in the build chamber (toward the gas inlet). After each printing cycle, these deposits were meticulously collected for study with various oxygen concentrations in the processing gas under investigation.

6.1.3 PBF-LB Processing of Hastelloy X

Paper VI is based on the investigation of the effect of powder layer thickness on spatter generation and oxidation during the processing of HX alloy in PBF-LB. For this investigation, EOS GmbH (Electro-Optical System) provided gas-atomized Hastelloy X (HX) powder with particle size distribution of 19 μm (D10), 35 μm (D50), and 58 μm (D90) with alloy composition according to UNS N06002. This alloy has Cr-level of maximum 23 wt% and elements like Al and Ti are nominally below 0.5 wt% and 0.15 wt%, respectively.

In an EOS M290 machine, the HX alloy powder was processed, and samples of the spatter were gathered from the gas outlet. Three builds were carried out utilizing nominal layer thicknesses of 80 μm , 120 μm , and 150 μm to examine the impact of powder layer thickness on spatter formation and hence in turn oxidation. The process parameters were tuned [45] and included a laser power of 370 W, a scan speed of 900mm/s, and hatch spacing of 0.1 mm to

obtain completely dense material. The utilization of a 67° rotation between subsequent layers during a layer scan approach was done. The parts were scanned in a way that was optimum for the flow of inert gas, with the first scanned parts being the ones that were placed the farthest from the gas entrance. In all three builds, the gas flow parameters were left unchanged. After the builds were finished, spatter samples were meticulously taken from the top of the machine's gas outlet, which is the part that allows gas to leave the build chamber and is depicted in our prior article.

6.1.4 PBF-LB Processing of TiAl6V4

In this thesis, two articles (papers VII and VIII) are based on the analysis of spatters from TiAl6V4. In the first study, the effect of layer thickness on generation and oxidation was investigated. In the second study, the effect of processing gas on generation and oxidation was investigated. Fresh plasma-atomized Ti6Al4V powder (AP&C, GE Additive) was used as feedstock material and was processed in an EOS M290 (EOS GmbH) PBF-LB machine. The particle size distribution measured by laser diffraction with a Mastersizer 3000 (Malvern Panalytical) was characterized by a D₁₀ of 23 μm, D₅₀ of 33 μm, and D₉₀ of 48 μm (average values obtained from 5 measurements). The build jobs conducted were identical and conducted under three high-purity atmospheres with less than 40 ppm impurities: pure Ar, pure He, and a mixture of Ar and He under the commercial name ADDvance® Laser230 by Linde AG. The properties of these gases are presented in Table 56. In an additional study, two different layer thicknesses of 30 μm and 60 μm were used to analyze the effect of layer thickness on spatter generation. After all build jobs were completed, spatters were carefully collected at different positions in the build chamber, namely, on top of the gas inlet, on top of the gas outlet, and in the gas outlet.

Table 5: List of gas properties employed in this work (internal data of Linde).

Gas	Density (kg/m ³)	Specific heat capacity at constant pressure (J/(kg·K))	Thermal conductivity at 25°C (W/(m·K))
Ar	1.62	520	0.016
ADDvance® Laser230	1.18	734	0.035
He	0.16	5190	0.142

6.1.5 PBF-EB processing of Alloy 718

Commercially available pre-alloyed Alloy 718 powder made by plasma atomizing wire in an argon environment was used as the material processed for this investigation. Table 7 provides information on the Alloy 718 utilized in this investigation. The powder's range in particle size was 45 to 105 μm.

Table 6: The composition of the Alloy 718 powder used in this study

Elements	Ni	Co	Cr	Mo	Ti	Mn	Nb	Ta	Al	Fe	Si	C
Wt.%	54.1	0.04	19.0	2.99	1.02	0.12	4.97	<0.01	0.52	17.12	0.06	0.03
At.%	53.38	0.04	21.16	1.80	1.23	0.13	3.10	<0.01	1.12	17.75	0.12	0.14

The powder was processed using an Arcam EBM A2X machine at GE Additive in Gothenburg, Sweden, and heat shields discarded after the process are used in this study. In PBF-EB machines, heat shields are employed to insulate the surrounding machinery from the effects of temperature and vapor condensation. The 316L stainless steel sheets are typically used to create heat shields. The sheets utilized in the current experiment were 35 cm tall and processed Alloy

718 powder over the course of 100 hours. Before lighting up the electron beam, a high vacuum of 10^{-5} mbar was established in the chamber to get rid of any remaining oxygen and prevent powder oxidation. He gas (grade 5) was added during processing, raising the pressure to 10^3 mbar. To pre-sinter the powder cake, improve conductivity and prevent the smoking effect, the powder bed temperature is kept at $1,000^{\circ}\text{C}$. To prevent contaminating the sheets, all four heat shields were carefully removed after a build cycle lasting 100 hours on the machine. These sheets were also used to gather the condensate and spatter for characterization.

6.2 Characterization techniques

6.2.1 Bulk chemical analysis

Bulk chemical examination of the powder is crucial to determining the rate of powder deterioration over time and to estimating the oxygen pick-up from virgin powder to spatter particles. The measurement of the change in O and N throughout the processing of powder is thought to be essential given the existence of residual air, especially in the PBF-LB process.

At Höganäs AB, combustion gas analysis with LECO ON836 was used for examining the chemistry of the powder. The inert gas fusion (IGF) theory underlies the combustion analysis, and samples are weighed before being put in a graphite crucible. The graphite crucible is transferred to the furnace, where the flow of He gas regulates the inert atmosphere. There, the temperature is raised to 3000°C , and when the sample melts, the crucible's walls are reacted with. When the sample's oxygen reacts with the graphite, CO and CO_2 gas molecules are created. The produced gas is passed via the detector (non-dispersive infra-red cells) at the gas outlet, where the detector uses infrared light to assess the absorption of CO and CO_2 gas molecules and calculate the quantity of oxygen in the sample. Using a thermal conductivity sensor, the nitrogen (N_2) that is released as N_2 molecules is found.

6.2.2 Microscopy

6.2.2.1 Scanning Electron Microscopy (SEM)

The LEO Gemini 1550 (LEO GmbH) SEM apparatus was utilized for the examination of powder morphology, microstructure, and fractography where secondary electrons were gathered using an in-lens detector. In-Lens detectors, which detect the secondary electron directly created by inelastic contact of the input electron beam and carry the greatest spatial resolution information, are frequently utilized in contemporary high-resolution SEM systems [87]. To prevent any contact and drift caused by carbon tape, the powder sample was generated by mounting the powder particles on the surface of an Indium metal plate.

Here, an electron beam emitted by a source (the SEM employed in this work uses a field emission gun as a source) striking the surface of the samples travels through several electromagnetic lenses and produces various signals [88]. The energy of the incoming electron, which is typically variable between 3 kV and 30 kV, may be used to regulate the strength of the produced signal. Depending on the beam intensity, material type, and incidence angle, the incidence beam interaction volume can range from a few microns to several.

As seen in Figure 14, SEM is a very dynamic analytical method that produces a variety of signals containing various amounts of information about the sample. The interaction of the electron beam with the specimen's electrons is related to the formation of these signals. In general, there are two different kinds of interactions: elastic and inelastic. In an inelastic interaction, the main electron from the incoming beam ionizes the specimen's atoms, which

then knocks out the secondary electrons. Due to the low energy of these electrons (~50 eV), electrons ejected close to the surface can only be detected. Therefore, the analysis of the topology and morphology of the specimen benefits greatly from the detection of the secondary electron. In contrast, after engaging with the atoms in an elastic interaction, the electron bounces back and such electrons are called Backscattered electrons (BSE). In comparison to secondary electrons, these electrons may have a larger interaction space in the material, as seen in Figure 14. Depending on the atomic number of the elements present in the material, BSE intensity fluctuates (a higher atomic number means more BSE). As a result, heavier elements look brighter in BSE mode than lighter ones do, and chemical contrast is provided by analysis. Finally, when the specimen's ionized atoms return to their normal configuration by shifting electrons from outer to inner shells, more energy is released during this process. X-rays are released as a result of energy generation. When the detector concept is utilized, the energy of the produced X-rays can be used to analyze the presence of different elements in the material. This technique is known as energy-dispersive spectroscopy.

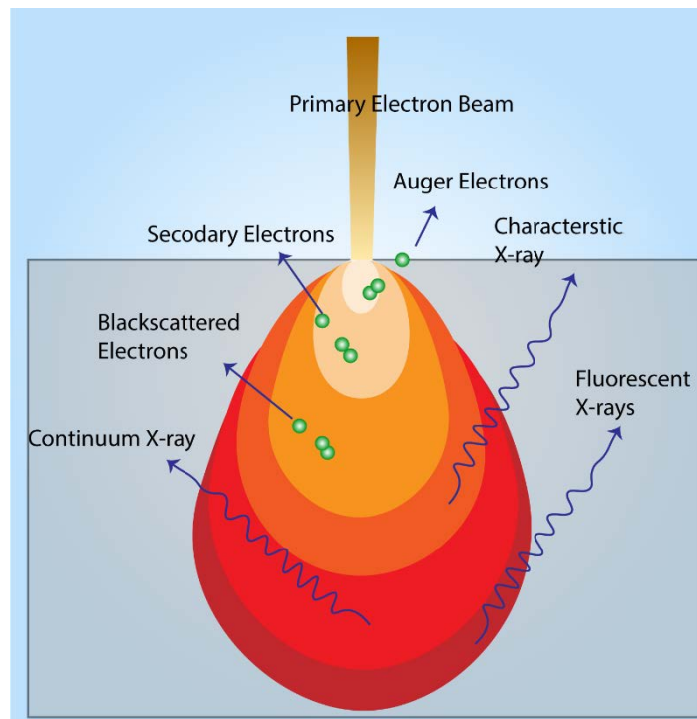


Figure 14: A schematic diagram depicting the interaction of the electron beam with the specimen generating various signals during SEM analysis.

6.2.2.2 Transmission Electron Microscopy (TEM)

The TEM is an effective instrument for examining the crystal structure of various phases present in the material together with their shape and chemistry at the nanoscale. In the current work, the microstructure and oxide scale on spatter particles were examined using an FEI Titan (FEI/Thermo Fisher Scientific, UK) coupled with a Silicon Drift (SSD) EDX detector (Oxford Instrument, UK). For the investigation of oxide shape and composition, TEM was run in scanning transmission electron microscopy (STEM) mode at 300 keV with the sample tilted at 15 degrees in the direction of the EDX detector. Using the FEI Versa3D focused ion beam (FIB) milling equipment, a sample with a typical 100 nm thickness was created for TEM analysis.

In TEM an image is produced when an electron passes through a substance. To get a very high spatial resolution of the sample, the electron beam can attain wavelengths that are much smaller than those of light. In TEM, an electron beam with extremely high energy (often 100–300 kV) is focused by a succession of electromagnetic lenses and directed toward the sample. A picture is taken on a phosphor screen or using a charge-coupled device (CCD) camera after the electron passes through the sample and is focused by the objective lens.

STEM combines the principle of both SEM and TEM. Like TEM, it requires a thin sample for analysis. A major advantage of STEM over TEM is that it enables the system to use the signals which can be spatially correlated in TEM e.g., secondary electrons, scattered beam electrons, characteristic X-rays, and electron energy loss, as shown in Figure 15. Like SEM, STEM scan the finely focused beam in a raster pattern over the surface of the sample, and interaction between the incident beam and the specimen generates a series of signals. These signals are correlated with beam position to create a virtual image where the signal level from any point on the specimen is presented by grey level. Scattered beam electrons are detected by a high-angle annular dark field (HAADF) detector to create a dark field image. High-angle annular dark field (HAADF) detectors use scattered beam electrons to produce dark field images. To assess the specimen's chemistry, incident beam contact generates X-rays that are collected by an EDX detector. Finally, electron energy loss spectroscopy (EELS), which offers information on surface features, elemental identity, electrical properties, chemical bonding, etc., analyzes the energy loss during transmission.

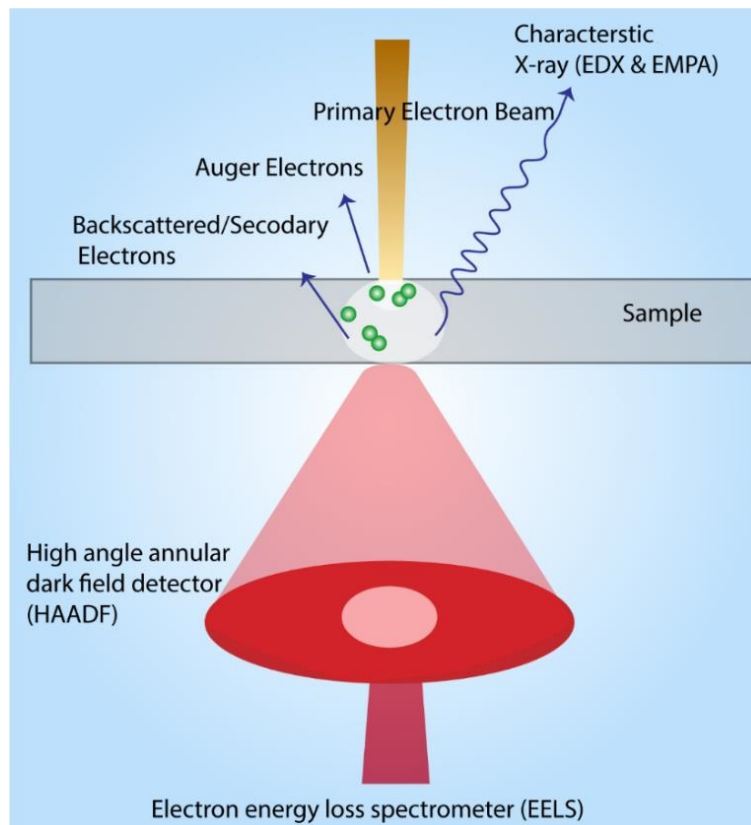


Figure 15: A schematic diagram depicting the interaction of the electron beam with the specimen generating various signals during TEM analysis.

6.2.3 Surface analysis

Powder degradation is often connected to the chemical changes related to the powder surface. Hence, surface analysis techniques like X-ray photoelectron spectroscopy (XPS), Auger electron spectroscopy (AES) and Nano-Secondary electron spectroscopy (Nano-SIMS) are useful tools to analyze surface properties. All three techniques were used to analyze the surface of the powders and spatter particles and a detailed description of these instruments is given in the following sections.

6.2.3.1 X-ray Photoelectron Spectroscopy (XPS)

XPS is a potent tool that can be used to analyze a variety of specimen surface characteristics (such as chemistry, chemical state, oxide layer thickness, type of oxide, etc.) with exceptional surface sensitivity resolution (10 nm) [89–92]. As the name implies, photoelectrons are produced for study using X-ray photons. Figure 16 shows how the hitting electron beam on the Al/Mg anode produces X-ray photons. The photons that are produced have a range of wavelengths. To get reliable data, produced X-ray photons are often directed toward the object using a monochromator lens, which streamlines the photons with a single wavelength. The photons excite the electrons from the atoms close to the specimen's surface when they come into contact with it. After leaving the surface, these photoelectrons are caught by an energy analyzer, which then scans the electron energy scale before a detector ultimately catches the signal.

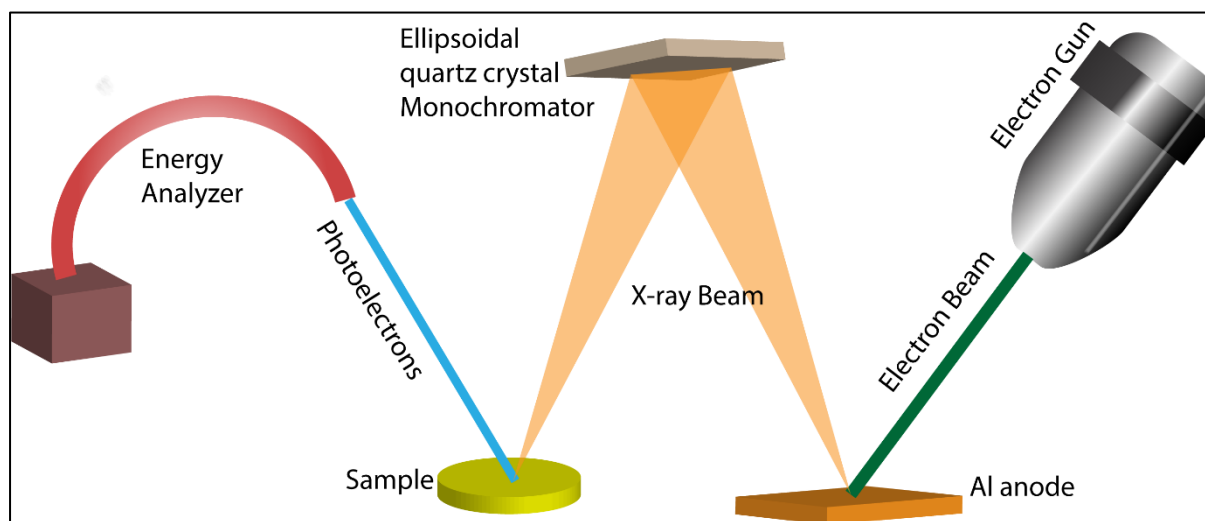


Figure 16: A schematic illustration of the XPS system.

The examination of photoelectrons and evaluation of the elemental composition follows a very straightforward mathematical formula. It is typically calculated from the binding energy (E_b) of detected electrons, which is obtained by deducting the work function (W) from the incident X-ray photon energy ($h\nu$) and the recorded kinetic energy (E_k) of detected photoelectrons. The correction for electron energy loss from exit to detection is the work function. The following equation can be used to represent the mathematical form:

$$E_b = h\nu - E_k - W \quad (1)$$

The data may be obtained primarily in two ways: through survey spectra and narrow spectra. When utilizing AlK α , survey spectra are conducted across a wide binding energy range (usually 0–1416 eV) to identify every element present on the specimen surface. Additionally, by

reducing the binding energy range and, thus, the energy resolution, narrow scan spectra are employed for extensive analyses of each element. For instance, for detailed analyses of oxygen, O1s spectra with binding energies ranging from 525 to 538 eV can be used. A further benefit of XPS is depth profiling, which allows the variation in chemical composition and chemical state with depth to be profiled. To do this, the top surface of the specimen is ion-etched using an ionized inert gas beam that is swept over the sample surface. Ion etching is done on the sample's surface to achieve this goal. Because core electrons in theory become stronger or weaker bonded to the nucleus depending on whether the element being investigated is in a cation or anion state, the measurement of chemical state utilizing the high-resolution narrow scan is one of XPS's strongest applications.

Utilizing the ULVAC-PHI 5500, X-ray photoelectron spectroscopy (XPS) was carried out. For the study, a monochromatic Al K X-ray source was employed. The analysis area was $300 \times 300 \mu\text{m}^2$, and powder samples for XPS analysis were attached on 3M tapes. The XPS data indicate a statistical average of around 20 to 30 particles due to the vast measuring area. Continuous ion neutralization was used to prevent the charging effect caused by the insulated nature of the template tape. To determine the oxide layer thickness, Ar⁺ ion etching was performed at a rate of around 5.2 nm/min. Ta₂O₅ overlayer with known thickness on Ta foil was used to calibrate the nominal etch rate. The pass energies used to collect the survey spectra and high-resolution narrow scans were 280 eV and 26 eV, respectively. Physical Electronics' MultiPak software was used to do the spectrum analysis. Utilizing the C1s peak at 284.8 eV that was discovered from beneficial hydrocarbons, the peak shift was corrected.

6.2.3.2 Auger electron spectroscopy (AES)

Auger electron spectroscopy (AES) is an effective surface-sensitive tool that can provide information related to surface chemistry on a scale of 1-5 atomic layers. The working principle of AES is like a typical SEM where a beam of electron strikes the surface of the sample and various kind of signals are generated which includes secondary electron, backscattered electrons, Auger electrons, and characteristics X-rays as shown in Figure 17. In principle, Auger electron are generated by a decay mechanism following the knockout of electron from a given shell by the incident characteristics X-rays generated during the process. Therefore, the energy of the Auger electron is usually limited in kinetic energy as in XPS and only the Auger electrons generated from the uppermost layers of sample can escape the surface. These electrons go into the detector which processed the data and generate peaks depending on the kinetic energy of the incoming electrons. The kinetic energy varies depending on the atomic number of the element and the electron levels involved in the Auger process.

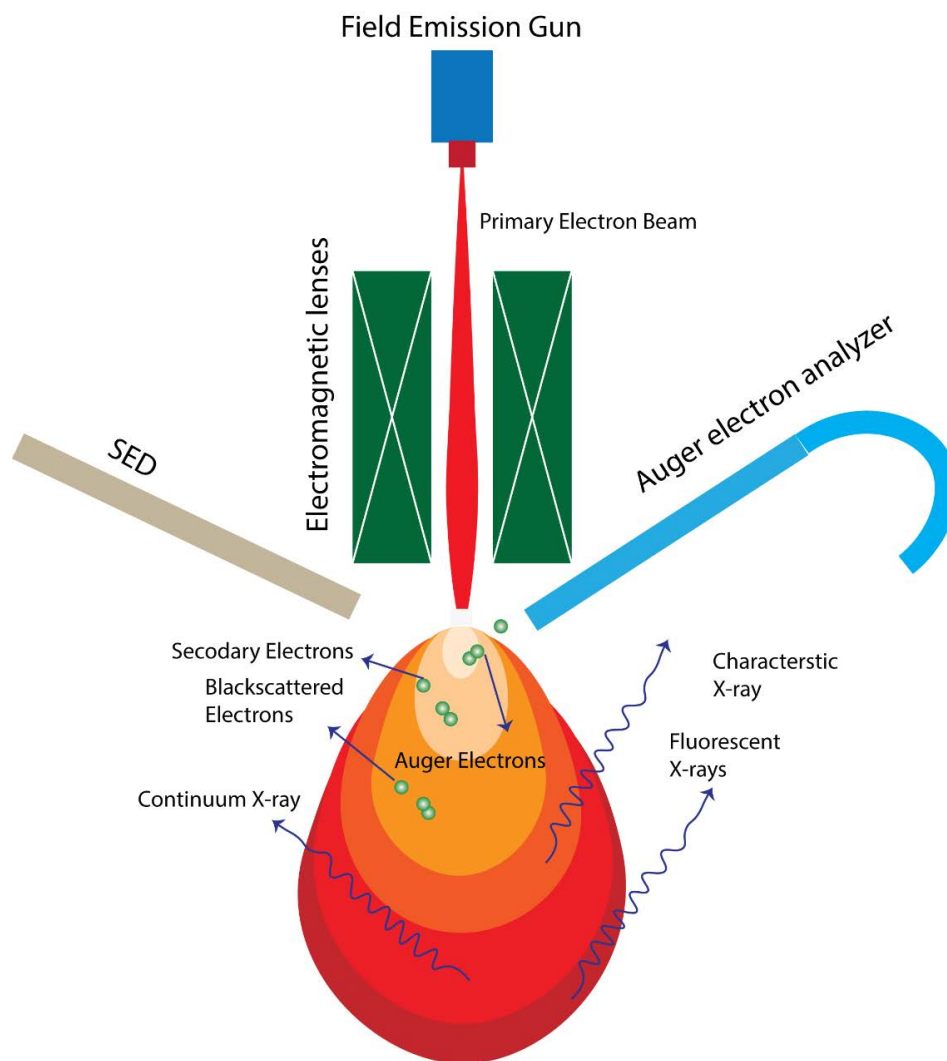


Figure 17: A schematic illustration of an Auger electron spectroscopy (AES) system.

Both XPS and AES techniques analyze the electrons with kinetic energies of less than 1500—2000 eV, which makes both very surface sensitive. The spatial resolution of AES is even higher than XPS. The benefit of AES over XPS is the presence of an in-built SEM system in the machine which can assist in seeing the localized areas on the sample which is not possible by imaging in XPS. However, XPS uses a monochromator source of X-rays to strike an X-ray beam with a single wavelength and resulting photoelectrons will be more quantifiable. Consequently, AES is more useful for qualitative analysis rather than quantitative analysis.

To learn more about surface chemistry, a PHI 700 AES from Physical Electronics was used for Auger electron spectroscopy (AES). The integrated SEM equipment helps in particle identification and surface examination with lateral resolutions up to 10 nm. The beam current was 10 nA, and the electron accelerating voltage was 10 kV, resulting in a nominal analytical lateral resolution of 10 to 20 nm. The depth profile investigation was carried out using Ar⁺ ion etching, which, like XPS, was done at a rate of 2.86 nm/min. The voltage utilized for the etching process was 2 kV, and the raster size was 3 mm². Samples with known Ta₂O₅ layer thickness on Ta foil was used to calibrate the etching rate. To prevent surface damage to the sample surface and improve conductivity, the powder samples were prepared by placing powder on an indium plate template. Image registration was carried out, and the analysis position was

calibrated every five cycles, to prevent drift during analysis. Physical Electronics MultiPak software was used for analyzing the data.

6.2.3.3 Nanoscale secondary ion mass spectrometry (Nano-SIMS)

Nano-SIMS is another surface-sensitive analytical tool to depict surface chemistry. In contrast to XPS and AES, Nano-SIMS uses ions as the primary energy source which strikes on the surface of the sample and upon collision ejects secondary ions by the erosion of sample material. The ejected secondary ions go through a series of electromagnetic lenses where they can be separated based on the momentum of the ions. The momentum relies on the mass of the ions which helps to identify the type of ions present on the surface of the sample. Nano-SIMS is an extremely sensitive tool that can provide information regarding the isotope impurities in the specimen. For Nano-SIMS, the number of detectors is usually limited to five or seven detectors and the positioning of those detectors is performed before the actual analysis by using the calibrating specimens. The commonly used primary ion sources are Cs^+ and O^- which generate both negative and positive ions. The detectors have to be tuned on one of the settings to either detect positive ions or negative ions.

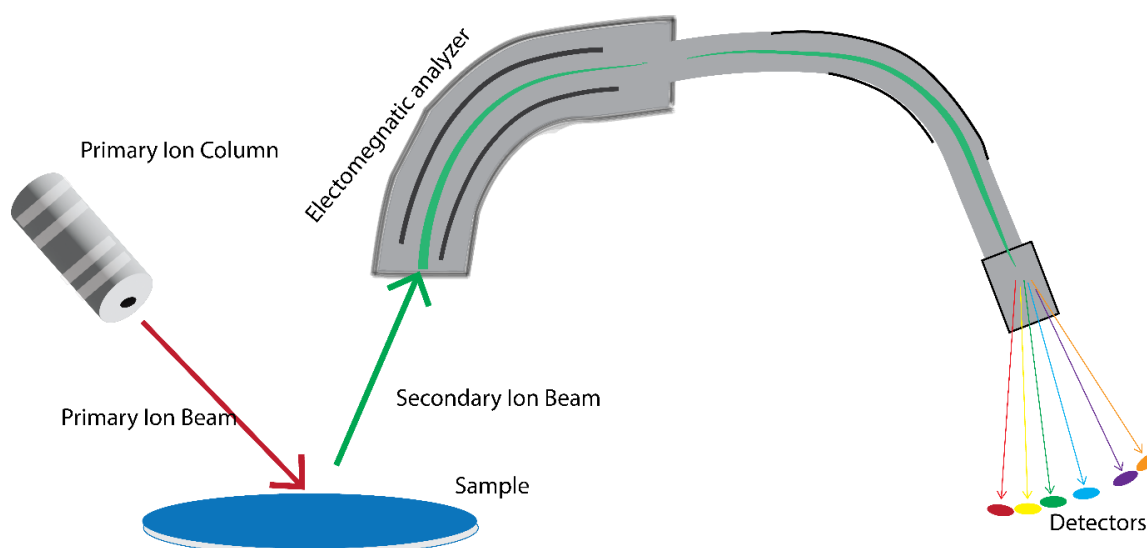


Figure 18: A schematic illustration of the Nanoscale secondary electron spectrometry (Nano-SIMS) process.

For this thesis work, the surface of virgin powder and spatters were further examined using nano secondary ion mass spectrometry (Nano-SIMS) using a cesium (Cs^+) gun, manufactured by Cameca Nano-SIMS 50, France, and having a spatial resolution of 50 nm. The information was gathered by sputtering with primary ions of Cs^+ at 20 pA in multidetector mode. The analysis employed ES3, AS2 slits, and D12 diaphragms with a field of view of $35 \times 35 \mu\text{m}^2$. The measurement's dwell duration was 1.5 ms. For the analysis, the materials were put on an Indium plate template. Nano-SIMS measurements were performed at the Infrastructure for Chemical imaging at Chalmers University of the Technology/University of Gothenburg.

7 Results & Discussion

This chapter is divided into two parts. Firstly, the research findings have been summarized regarding the research questions, whereas the second part is based on the synopsis of appended papers.

7.1 Summary of research questions

RQ1: What is the dominant powder degradation mechanism in the PBF-LB process?

To determine the dominant mechanism contributing to powder degradation, a study was done on AlSi10Mg powder processed for 30 months in a closed-loop machine. The careful analysis of the samples from reused powder showed that highly oxidized spatters mainly contributed to the oxidation of the powders. The spatter particles had a thick oxide layer with thickness varying from 75-125 nm. To validate the conclusions from the study on AlSi10Mg with other alloys, the analysis of spatters from Alloy 718, HX alloy, and TiAl6V4 was conducted. The results showed that spatters from different alloys oxidize differently, but it remains the main powder degradation mechanism in all different alloy systems during the processing of PBF-LB. Papers I-V are concerned with RQ1. A summary of these papers is available in the next section.

RQ2: What is the effect of part geometry and processing parameters on the generation and properties of spatter during PBF-LB?

To determine the effect of part geometry, capsules containing lattice structures with varying density and overhang structures were built. The results showed that the overhang structure and lattices with higher thickness generates more spatter and designing them smartly can reduce the generation (Appended paper III provides detail regarding this). The effect of powder layer thickness on the generation of spatters was evaluated and the findings showed that greater layer thickness results in a higher number of hot spatters. Further analysis showed that the overall cumulative amount of hot and cold spatters decreases with an increase in powder layer thickness (Appended paper IV and V discusses this).

Regarding process parameters, the effect of processing gas was also investigated where argon, helium and a mixture of argon and helium gases were used. The results showed that the introduction of He in the processing atmosphere can reduce the number of generated spatters by up to 70% (appended paper VI). Furthermore, to evaluate the effect of processing gas purity on spatter oxidation, the varying residual oxygen content was applied. The findings showed that an increase in the purity of the build atmosphere can reduce the extent of oxidation of the spatters (Appended Paper VII).

RQ3: What is the effect of powder degradation on the properties of fabricated parts?

The effect of spatter redeposition on the powder bed was evaluated by a specially designed study. The results showed that the redeposition of spatters during a build job on subsequent parts can cause a lack of fusion defects (Appended Paper VIII). Further, the effect of prolonged powder reuse on porosity and mechanical properties was investigated. The results showed that prolonged powder reuse can result in an increase in porosity and a decrease in strength which was mainly linked to the accumulated number of spatters (Appended Paper IX).

RQ4: What is the dominant powder degradation mechanism in the PBF-EB process?

The processing conditions in the PBF-EB process are dynamically different from the PBF-LB process. The PBF-EB process works on a significantly higher temperature and higher vacuum level. A study on the rheology and surface chemistry of reused powder showed that powder flowability improves with reusability. However, significant powder surface oxidation was observed in case of the reused powder. An additional study on the sublimation aspect during the processing of Alloy 718 showed that volatile elements like Al and Cr got sublimated during the processing in PBF-EB. Still, oxidation of the powder was determined as the main powder degradation mechanism in the PBF-EB process (Appended Papers X, XI).

7.2 Summary of appended papers

Paper I

AlSi10Mg powders were reused for over 30 months in the XLINE 2000R machine, which has a closed-loop powder handling system under a controlled atmosphere. To analyze the degradation behavior of powders, samples were collected after 6, 10, 14, and 30 months of reuse and compared with virgin powder. A summary of the findings from this study is illustrated in Figure 19. Bulk oxygen analysis of the powder samples showed a sharp increase in oxygen content at the start from the virgin to Al6 sample, which stabilized after further reuse. This was an indication of the formation of a stable oxide layer on the surface of the powder that hindered further oxidation. However, morphology analysis showed that a few bright particles appear in the reused powder. High magnification analysis showed that the surface of these particles is covered with thick nodular oxide layer. Although the consumed amount of feedstock powder was cyclically top-up with virgin powder, the quantification showed that the number of spatter particles in the powder after 30 months of reuse reached up to ~3 %. This amount is significant considering the oxide layer thickness on the surface of these particles which varied from 50-125 nm.

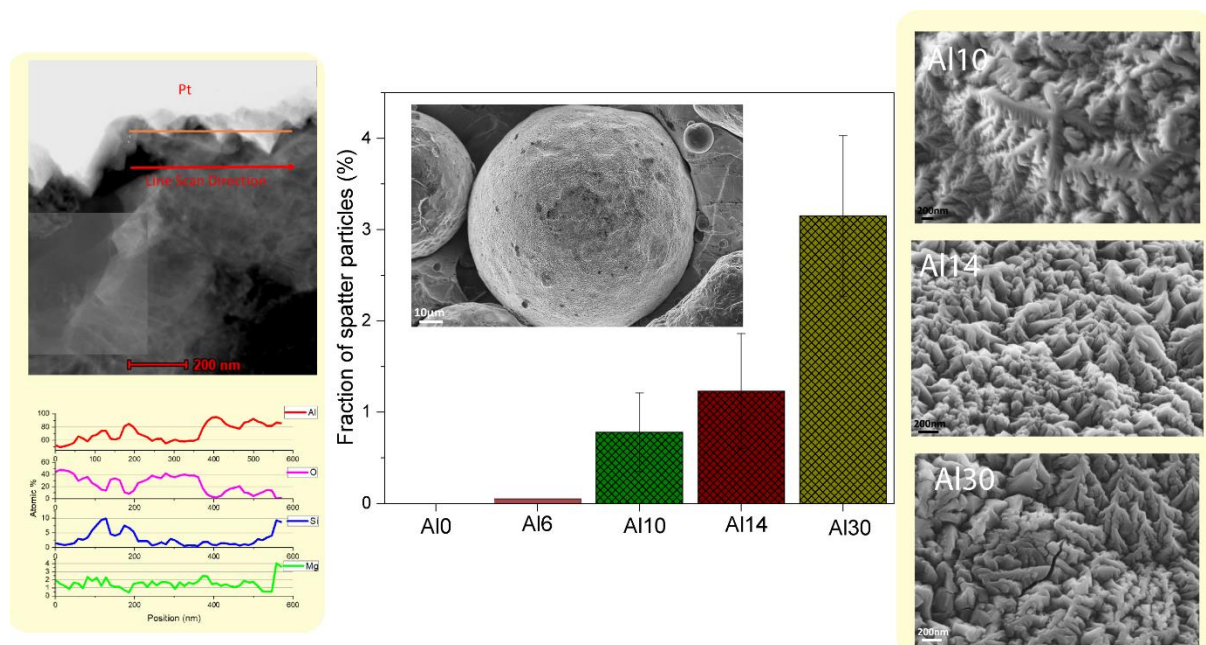


Figure 19: A summary of results where the central plot is showing the quantification of spatter particles in different samples. Whereas the SEM images on the right side are showing the morphology of spatter particles from the samples Al10, Al14, and Al30. Lastly, the images on the left end are the findings from the STEM-EDX analysis.

The STEM-EDX analysis confirmed the formation of wavy nodular oxide on the surface of spatter particles, where the oxide layer mainly consisted of Al-based oxide with a small contribution from Mg-based oxides. XPS analysis provided further evidence of the formation of Al_2O_3 on the surface of spatters along with a small fraction of the MgAl_2O_4 spinel phase. Thermodynamic calculations by CALPHAD tools reaffirmed the experimental results where calculations showed the possibility of spinel formation along with the Al_2O_3 oxide phase on the surface of spatters. Moreover, the analysis of data from XPS depth profile measurement showed that the oxide layer thickness increased from 4 nm to 38 nm from virgin to Al30 powders respectively. This increase observed in XPS data was strongly influenced by the presence of spatter particles with a thicker oxide layer.

Overall, the study showed that spatter strongly influences the extent of powder degradation. Moreover, it is essential to continuously monitor the quality of the reused powder during prolonged reuse to improve the reproducibility and robustness of the process.

Paper II

To verify the role of spatter formation on powder degradation during the processing of Alloy 718, a special set of experiments was planned where the spatters deposited on the gas inlet and outlet were carefully collected. The gas inlet and outlet are the points from where processing gas enters and exits from the build chamber as shown in Figure 20. The collected samples were further analyzed by bulk oxygen analysis, SEM, and XPS to determine the oxidation behavior of the spatters.

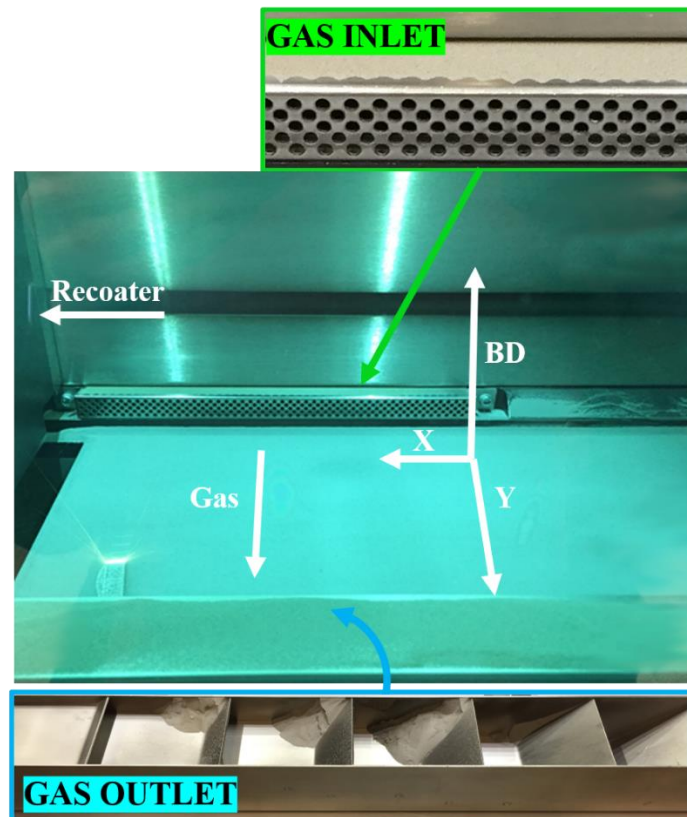


Figure 20: A photograph of the EOS M290 machine's build chamber. The insert images show both the gas inlet and outlet from where deposited spatter samples were gathered.

Analysis of the spatters collected from the gas inlet and outlet were compared with the virgin powder to benchmark the extent of degradation. The bulk oxygen analysis of spatters showed a 100 % increase in oxygen content compared to the virgin powder. The SEM analysis showed the formation of oxide particulates/patches on the surface of spatter particles. This oxidation mechanism of spatters from Alloy 718 is quite different from the oxidation mechanism of spatters from AlSi10Mg powder where the spatter surface was uniformly oxidized. XPS examination was done to describe the type, nature, and thickness of surface oxides. The study of the XPS narrow spectrum indicates that the predominant oxide particles and patches are Al- and Cr-based oxides, which is related to these elements' greater sensitivity to oxidation. When compared to the virgin sample, normalized oxygen content analysis revealed a significant increase in oxygen content at deeper etch depths, indicating a thicker oxide layer on these spatters.

A thorough microstructural investigation was carried out to better assess the thermal history of spatter powder in comparison to virgin powder. This study helped to distinguish the melt ejecta from the entrained spatter particles (entrained particles are affected by laser but not fully molten). The examination revealed that the entrained particles, which resembled fresh powder, had both primary and secondary dendrites. The melt ejecta, however, exhibited no secondary dendrites and only primary dendrites. This discrepancy is related to the different cooling rates experienced in the PBF-LB build chamber and atomizer. Calculations of the solidification rate revealed that the melt ejecta cooling rate in the PBF-LB system was one order of magnitude higher than that encountered during atomization. The findings also showed that entrained particles with partly heated or melted surfaces made up most of the spatter particles that were collected at the gas inlet and outlet. The observed oxidation in the form of patches and particulates was caused by the partial heating and/or melting of entrained particles.

Paper III

To evaluate the effect of part geometry on spatter formation, redeposition in the powder bed, and powder degradation, a simulated study was designed. For this simulated study, special capsules were designed with varying lattice geometry. Special capsules with various lattice geometry were constructed for this simulated investigation. The build job consisted of empty (E), L7D1, L7D3, and L3D1 capsules. Here, L stands for the length and D for the lattice struts' diameter (both in millimeters). The surface-to-volume ratio and the quantity of specific heat in the capsules were both intended to be altered by the lattice arrangements. During fabrication, heat and byproduct signals from the scanned region were tracked using in-situ optical tomography (OT).

According to the OT analysis, compared to an empty container, capsules with the lattice dimensions L7D3 and L3D1 displayed more grey value (GV) signals, as shown in Figure 21. This was caused by the capsules' denser and thicker lattice geometries. The design with a big surface-to-volume ratio (L3D1) and a large area of overhangs has a higher propensity to produce by-products, according to larger GV signals. The L7D3 and L3D1 samples had a larger number of spatters, according to the SEM examination of powder samples taken from capsules, which is consistent with the results of the OT data analysis.

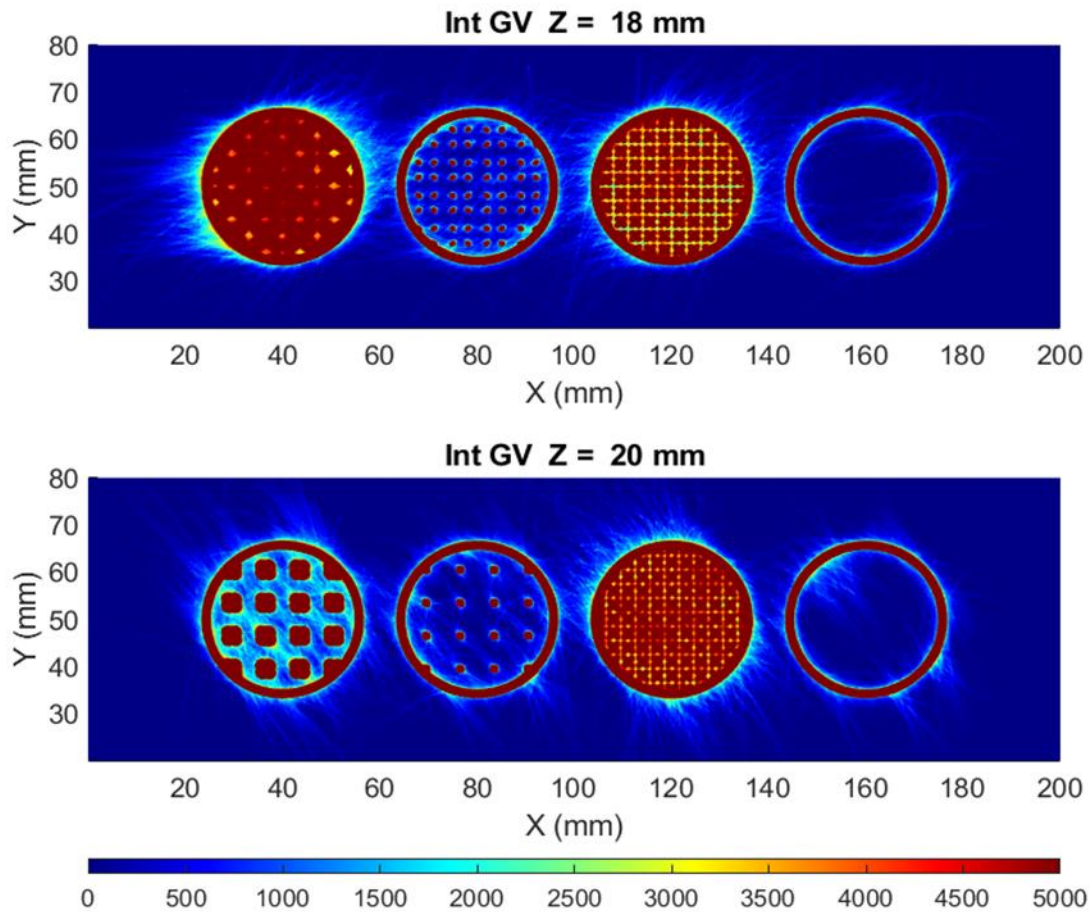


Figure 21: OT images at two build heights. The color scale for GV's is customized to highlight the occurrence of process byproducts (spatters) (OT analysis was performed by Z. Chen).

The collected samples were subjected to oxygen content and XPS analyses to correlate OT findings with powder chemistry and surface chemical composition. The examination of oxygen content revealed no appreciable difference in oxygen content between the virgin powder and the empty and L7D1 capsules. The samples obtained from L3D1 and L7D3 capsules, however, showed a 22% and 49% increase in comparison to virgin powder, respectively. The increased quantity of spatter buildup in these capsules is what caused this rise. Like how the virgin powder was affected by the presence of spatter particles, XPS research revealed that the normalized oxygen content rose in L3D1 and L7D3 capsules at higher etch depth in comparison to the virgin powder.

In conclusion, the investigation showed a strong correlation between by-product production and part geometry. The amount of by-product buildup also revealed information on the powder's deterioration.

Paper IV

To relate the oxidation behavior of spatters from HX alloy and determine the effect of layer thickness on the amount of spatter generated during the process, a study on HX alloy was conducted. During the processing of HX alloy, the built parts were divided into 3 sections where powder layer thickness was varied to 80 μm , 120 μm , and 150 μm . The spatters were collected from the gas outlet and analyzed using SEM, XPS, and AES.

The OT data analysis by hot signals determined by grey values show that the number of hot spatters increased with the increase in the layer thickness of powder, see Figure 22. Moreover, the number of spatters deposited on the powder bed increased with an increase in powder layer thickness, but with different intensity across the build plate . A noticeable aspect here is that the OT images only observe the hot spatters, and are not representative of cold spatters. Still, this represents the spatters which will be most affected by heat and exposure to the atmosphere.

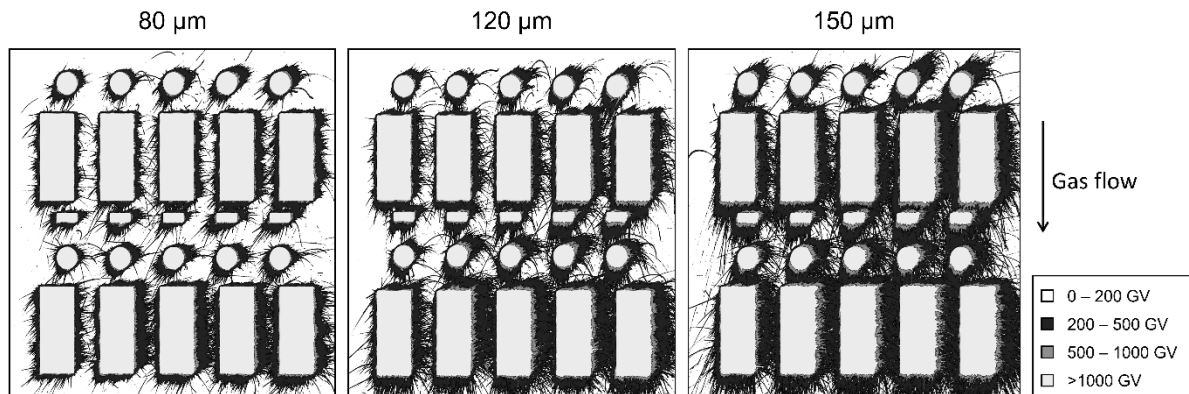


Figure 22: Contour plots of the signal intensity registered via OT of a single representative layer of builds performed with nominal layer thicknesses 80 μm , 120 μm , and 150 μm .

The SEM analysis of the spatters displayed that the spatter can be divided into three groups depending on the surface morphology of the particles. The AES analysis elucidated that the nature and composition of oxides on the surface of the spatter particles vary from one another. The XPS analysis highlighted that the surface enrichment of various oxide-forming elements varied with the layer thickness. The enrichment of Al- and Ti-based oxides was lowest in the spatters generated at 80 μm , and it scaled with the nominal powder layer thickness. The average oxide layer thickness also increased with powder layer thickness from ~ 2.5 nm in virgin, ~ 45 nm in 80 μm , ~ 55 nm in 120 μm , and ~ 68 nm in 150 μm powder layer thickness spatter sample, as shown in Figure 23. Thermo-Calc calculations further supported the experimental findings, where Al- and Ti-rich corundum and Fe- and Cr-rich spinel formation was evident.

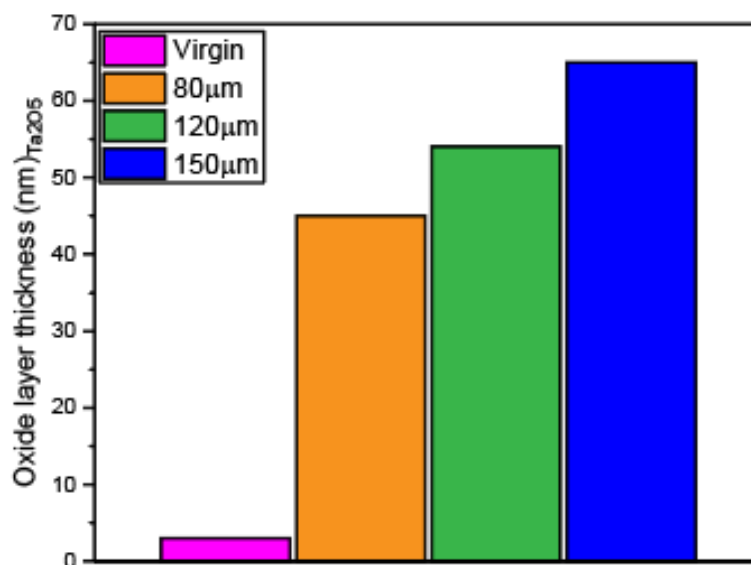


Figure 23: Comparison of the oxide layer thickness of spatters generated at 80 μm , 120 μm , and 150 μm with the virgin powder.

Paper V

To further understand the effect of powder layer thickness on the stability of melt-pool as well as to comprehend the mechanism of oxidation of TiAl6V4, a similar study to HX alloy was done on TiAl6V4. Here the thickness of powder layer thickness was varied between 30 μm and 60 μm in an inert argon gas atmosphere. Figure 24 summarizes the findings from this study where the overall amount of spatter particles decreased by up to 40 % increase in layer thickness from 30 μm to 60 μm . Compared to the virgin powder, the oxygen content of the spatter was more than 1000 ppm (or around 60%), while the nitrogen content was more than 200 ppm higher.

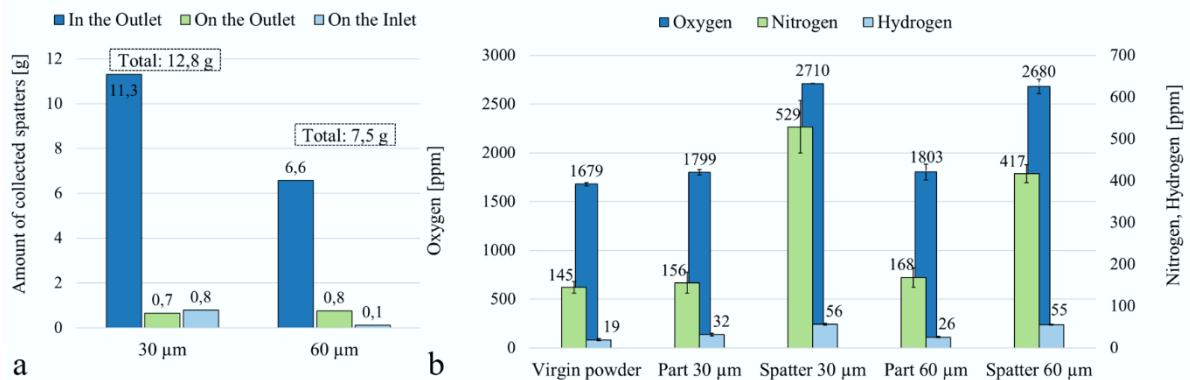


Figure 24: (a) Comparison of the amount of collected spatters for the 30 μm and 60 μm layer thickness build jobs. (b) Oxygen, nitrogen, and hydrogen contents were measured in the Ti-6Al-4V virgin powder, the built parts and in the spatter collected in the outlet after the 30 μm and 60 μm layer thickness build jobs.

The thickness of the oxide layer determined by XPS analysis is approximately doubled compared with the virgin powder. The analysis of spatter morphology and chemistry indicate the same characteristics of spatter particles and hence suggests that the spatter generation process for the 30 and 60 μm layer thickness is the same. In addition, the spatter particle size being very similar to the virgin ones would directly be responsible for the conservation of these degraded particles within the processing chain and hence in the printed components, resulting in oxygen and nitrogen pick-up as well as bringing the risk for increased content of non-metallic inclusions. The study suggested that the greater layer thickness is promising not only from the productivity perspective but also has a positive impact on powder reusability and thereby overall sustainability of PBF-LB processing of Ti6Al4V.

Paper VI

In terms of process parameters, processing gas can also play an important role in spatter generation and oxidation. To evaluate the effect of chamber atmospheric gases on spatter generation and oxidation during the processing of TiAl6V4, three different atmospheres were used including Ar, He, and Ar+He mixture. A graphical summary of this study is illustrated in Figure 25. The results showed that 70% more spatters were generated during the processing in the Ar atmosphere compared to the He-Ar atmosphere which can also be observed from the graph given in the top left corner in Figure 25. The oxygen pickup showed similar results where spatters generated in the Ar atmosphere showed the highest oxygen pickup followed by mixture (Ar-He) and pure He atmosphere.

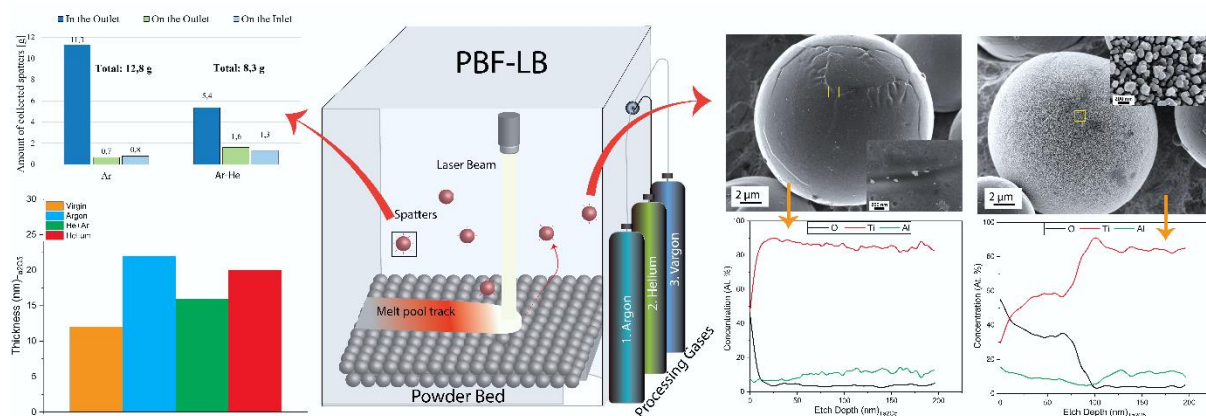


Figure 25: A graphical summary of the study covering the amount of spatter in the top left corner, the oxide layer thickness increase in the bottom left graph. While the plots on right are the results obtained from AES.

When the morphology of spatters and virgin powder were compared, it became clear that oxide nanoparticles were forming on the spatter surface that was not present on the virgin particles. The spatter particles also underwent varying degrees of oxidation, with some spatters having granular oxide scales on their surfaces. According to XPS examination, Ti-based and Al-enriched oxide layers made up the majority of the oxide scale. The fact that the Al-rich oxide layer was thicker than the uniform oxide layer suggested that Al-rich oxide particles had formed. The average oxide layer thickness determined by XPS analysis also revealed that the oxide layer thickness nearly doubled from the virgin powder to the spatters collected in the argon atmosphere, from 7.2 nm for the virgin powder to about 13.5 nm, 11 nm, and 12 nm for the spatters sampled during PBF-LB processing in Ar, Ar-He, and He, respectively. Based on the origin of the spatters and the way they interacted with the laser and melt pool, the AES analysis revealed that the level of oxidation of the spatters varied. Granular oxides, which form oxide scale on the spatters and are identified by AES analysis, are composed of mixed Al-Ti oxides. The Nano-SIMS study demonstrated that the spatters have substantially greater enrichment in Al-oxide than the virgin powder, which is coated with a thin oxide layer made up primarily of Ti-based oxide with some Al-oxide. Al- and Ti-based oxide information overlaps suggesting the presence of mixed oxides.

According to this study, the processing gas has a significant impact on both the quantity of created spatters and the degree of oxidation. The addition of helium gas to the environment can significantly lower the quantity of created spatters as well as the degree of spatter oxidation due to helium's increased thermal conductivity. Based on the harmful impact of spatters on powder reusability, this has a substantial influence on the enhancement of powder reusability and therefore enables the PBF-LB process to be more affordable, durable, and sustainable.

Paper VII

Earlier studies have evaluated spatters and different parameters which can influence/reduce spatter generation. This work is focused on reducing the extent of spatter oxidation by controlling the residual oxygen content in the chamber. The oxygen partial pressure was closely monitored by an external system, the ADDvance®O2 precision (Linde GmbH), and was changed from 20 ppm to 1000 ppm to assess the impact of the residual oxygen content in the process chamber on the degree of spatter oxidation. The samples were taken from the gas inlet, where the majority of the entrained spatter particles are present. The deposited spatters on the

gas intake are seen in Figure 26, where a distinct powder discoloration is associated with the rise in oxygen content from a grey to brown look. This discoloration is related to how much the spatter is oxidizing, which is happening more and more as the chamber's residual oxygen level rises.

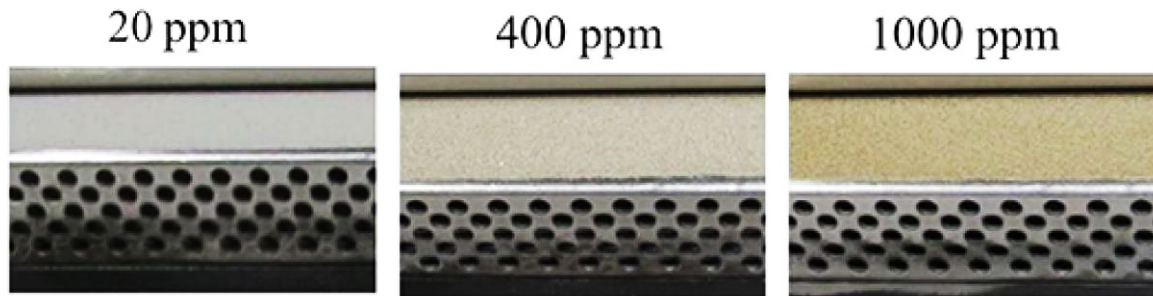


Figure 26: Deposited spatters on the gas inlet, where a distinct discoloration with rising in residual oxygen content in the process atmosphere can be observed.

The examination of the bulk oxygen revealed a relationship between oxygen pick-up and residual oxygen content. Approximately 30% more oxygen was found in the sample taken at 20 ppm of oxygen compared to the virgin sample. The increment was more evident for increased O₂ partial pressure, and a gain of about 300% in oxygen content was detected for the sample collected under the usual working level of most PBF-LB machines, which is 1000 ppm residual oxygen. Analyzing the morphology of the samples that were gathered, as shown in Figure 27, also makes this alteration quite evident. Thin oxide patches can occur when the oxygen level is decreased. However, the oxide patches thicken as the remaining oxygen level rises, and oxide particle production was also seen.

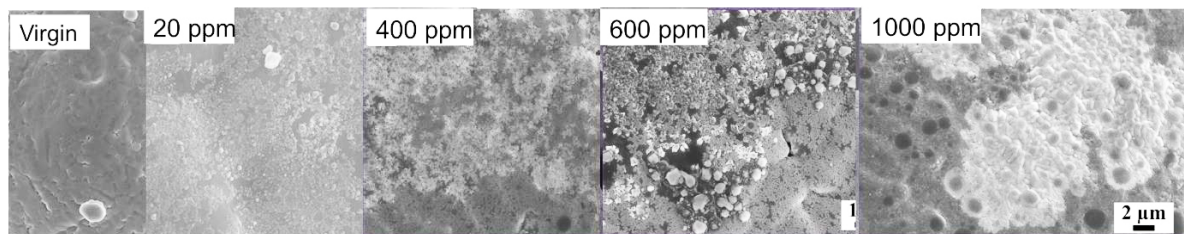


Figure 27: Morphology comparison of virgin powder with the spatter particles gathered at varying residual oxygen content varying from 20 ppm, 400 ppm, 600 ppm, to 1000 ppm.

The surface was mostly covered by Al- and Cr-based oxides, as revealed by the XPS survey spectra and narrow spectra analyses. Al was shown to be a predominantly oxidized at a lower oxygen level than Cr by fitting the O1s and Cr2p_{3/2} spectra. In comparison to Al, the Cr contributed very little to the oxide layer at 20 ppm O₂. However, when the amount of residual oxygen increased, Cr also started to mostly oxidize with Al. Thermo-calc and Dictra calculations were used to further describe this observation, and they revealed that Al can oxidize with far less oxygen than Cr. According to the normalized oxygen content calculation, when the residual oxygen content increases, there is a significant rise in oxygen content at greater etch depths, as shown in Figure 28a. From 20 ppm (15 nm) to 1000 ppm O₂ (75 nm), the thickness of oxide patches and particles also dramatically increased (Figure 28b). The oxide layer thickness determined using O1s is contrasted with the oxide layer thickness obtained from Cr2p_{3/2} narrow XPS spectra. This suggests that compared to Cr, Al-based oxide patches are thicker.

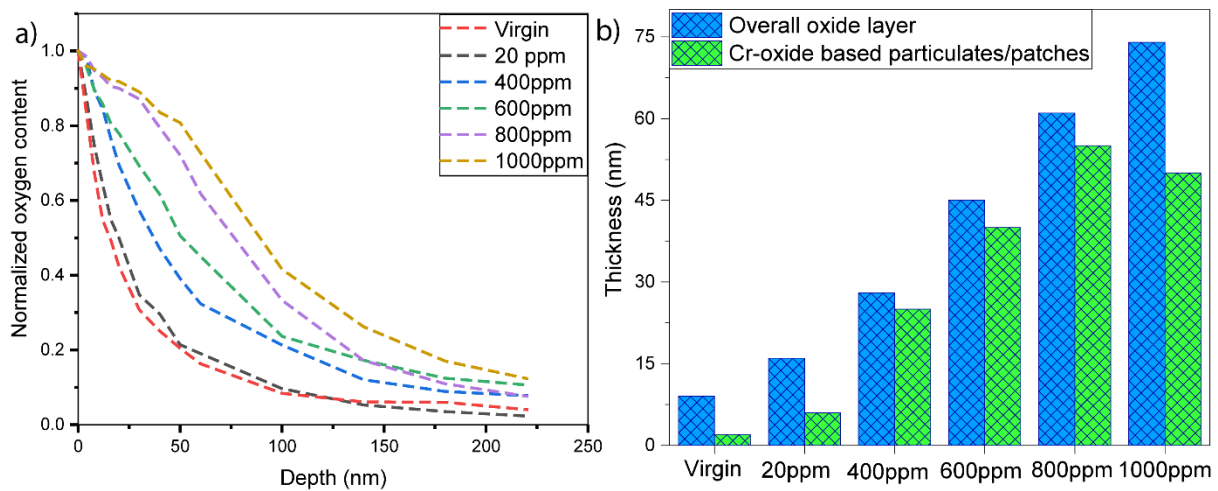


Figure 28: a) Normalized oxygen content comparison of all the samples and b) Estimated Cr-based oxide particulates/patches thickness from $\text{Cr}2\text{p}_{3/2}^{\text{met}}$ and overall oxide layer thickness calculated through O1s spectra of all samples.

Paper VIII

To evaluate the effect of spatter redeposition, study with higher layer thicknesses, leading to more intensive spatter generation and hence re-deposition on build parts, was conducted. This paper is entirely focused on the number of depositions on subsequent parts and their role in defect formation. The results in appended paper VIII showed that the increased redeposition of spatters on the powder bed increased the amount of lack of fusion of defects. Two factors were influencing this phenomenon. Firstly, the size of the spatters was significantly bigger than normal feedstock powder which was hindering the complete melting. Secondly, the surface of spatter particles was covered with a thick oxide layer which results in defect formation due to the lack of cohesion. Figure 29 is showing the fractured surface of the sample fabricated with $150 \mu\text{m}$ layer thickness. Figure 29a shows a lack of fusion defect on the fractured surface where a large spatter particle with a size larger than $200 \mu\text{m}$ can be observed. A higher magnification image of this particle shown in figure 29b, which elucidates that the surface is covered with fine oxide particulates. The cumulative effect of spatter particle size and oxide layer over the particle surface hindered the complete melting and resulted in a lack of fusion defect. Such defects are particularly detrimental to the properties of the parts which are about to be used in dynamic applications where good fatigue properties are essential.

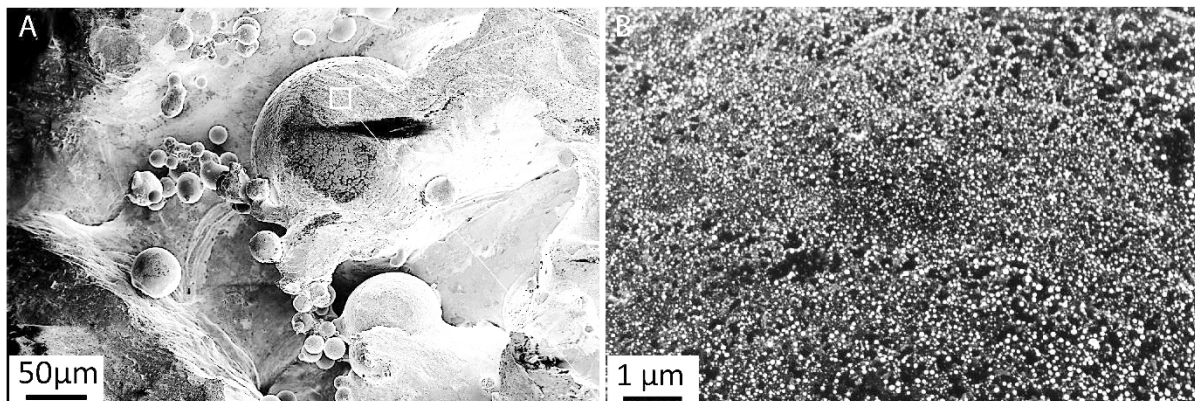


Figure 29: The fractured surface of the sample fabricated with $150 \mu\text{m}$ layer thickness.

Paper IX

In this study, the impact of powder degradation on microstructure and mechanical behavior—observed in the first appended paper based on an analysis of AlSi10Mg powder reused for more than 30 months—was assessed. The findings revealed a 13% drop in strength and an increase in porosity from 1% to 3%. Finding of the cause of the rise in porosity was the first goal of the inquiry. To assess this, the role and concentration of hydrogen in components made from both new and used powder were carefully observed. The phenomena of H₂ diffusion and segregation on defect sites followed by the development of porosity are well-known. The amount of hydrogen in the sample made from new powder (Al0) and the most recycled powder (Al30), however, was comparable in both cases (20 ppm). Therefore, the observed increase in porosity could not be attributed to hydrogen alone.

Additionally, the examination of the fracture surfaces revealed a distinct contrast between samples made from virgin and recycled powders. First, the presence of small dimples in both cases led to the identification of transgranular dimple ductile fracture as a common micro-failure mechanism (Figure 30). Large holes are also present in both cases, with a somewhat larger percentage of these flaws in the sample made from the reused powder. The biggest difference between the samples may be noticed at greater magnification, as shown in Figures 30 and 31, where the reused powder has a noticeable presence of oxide residues inside the pores, while the virgin powder does not. This highlights the part played by the surface oxide phases in the processed powder in the creation of defects during PBF-LB. Additionally, Figure 31c shows that the fracture surface of the samples made from the reused powder had thick and widespread oxide inclusions that extended dozens of micrometers. The detected difference in mechanical characteristics between the two materials is explained by the presence of such inclusions on the fracture surface in conjunction with regions of low matrix cohesiveness. As a result, the presence of oxide inclusions in the material as it is produced from the reused powder affects its mechanical characteristics: 1) through the existence of many inclusions, which weaken the material's interfaces and affect mechanical properties; an even greater influence on dynamic characteristics may be anticipated; and 2) by the presence of such interfaces, which promote the production of hydrogen pores and microporosity.

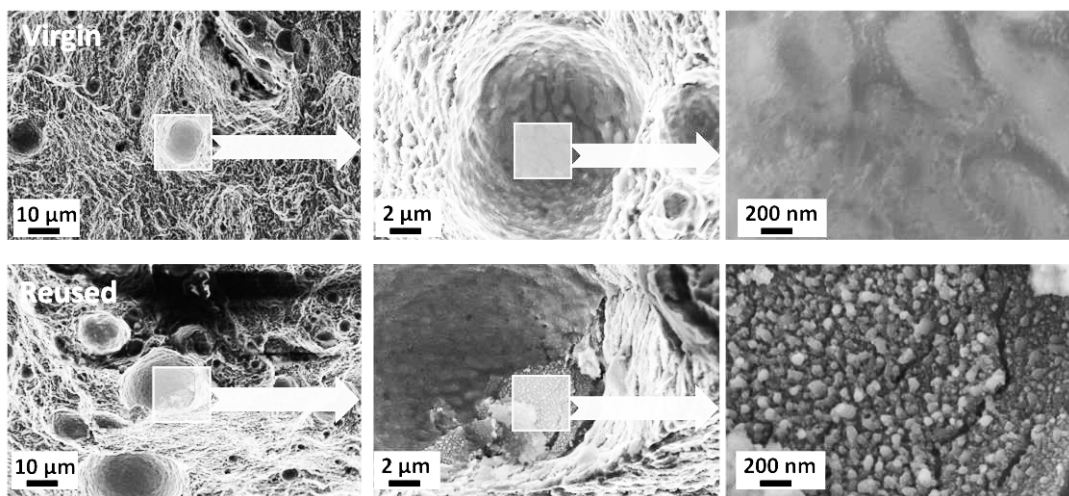


Figure 30: Fractography of the samples fabricated from (top) virgin powder and (bottom), reused powder showing the occurrence of oxide phases in the pores in the reused sample.

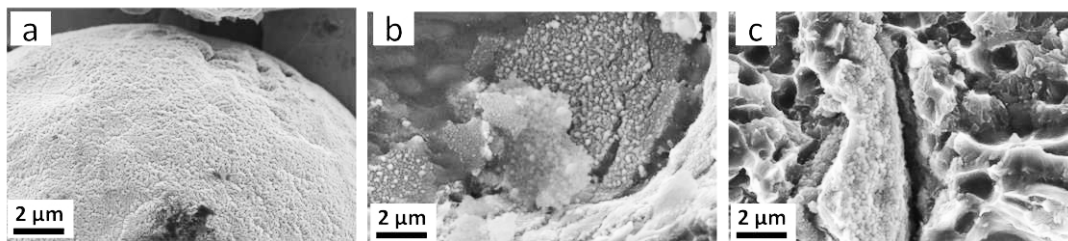


Figure 31: a) SEM images of the AlSi10Mg spatter particle and b) appearance of the oxide inclusions in the pore and c) extensive inclusion on the fracture surface of the component fabricated from this reused powder.

Paper X

To determine the dominant powder degradation mechanism in the PBF-EB process during the processing of Alloy 718, virgin and reused powder (causing smoking during build) were analyzed. During the analysis, rheology, surface chemistry, and surface charging behavior were analyzed to determine the reason behind the smoking of reused powder. As shown in Figure 32, the change in surface chemistry can affect electron dissipation during the processing. After being used again, the powder's overall oxygen concentration rose by 20%. From new to recycled powder, the oxide layer composition and thickness differ. Powder is covered by thin oxide layer, predominantly formed by Ni oxide with presence of Cr-oxide in it. According to the XPS examination, in the case of reused powder, the powder surface oxide was enriched in Al-rich oxide particulates with an average thickness of roughly 13 nm. When determined by dynamic flowability parameters using the RPA, reused powder displays enhanced flowability driven by changes in the oxide layer. For virgin and used powders, the loose volume fractions, which corresponds to packing density, are around 57% and 56%, respectively. The particles and varying surface roughness of the reused powder may be impeding further packing when the packed volume fraction taps to 60% in virgin powders and 57% in recycled powder. Reused powders have a different charging behavior (-9.18 V/g) compared to virgin powders (-5.84 V/g), which may provide less conducive electrical conditions for smoking in the powder bed.

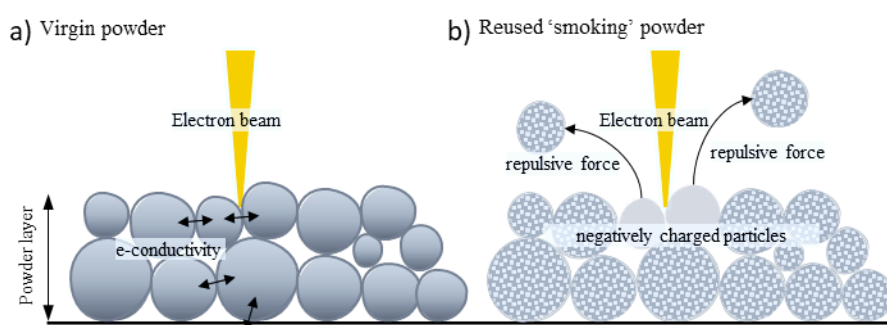


Figure 32: A schematic highlighting the effect of powder oxidation on smoking during LPBF-EB processing (from paper 10).

Paper XI

Heat shields, which cover the build area and protect the machine from heat effects and vapors, were examined to assess the sublimation happening during the PBF-EB process of Alloy 718. Sublimated vapors that settle on the surface of heat shields in the form of condensates and spatters cover the heat shield. The distribution of spatters and condensates on the heat shield's surface is shown in Figure 33. The bottom of the heat shield received preferential deposition of the condensates and spatters. Condensate reached a thickness of more than 50 μm at the

bottom but only 5 μm at the top. According to a particle examination of the spatter, the surface was covered with vapors of condensate, and the amount of deposited condensate on the spatter surface changed depending on how long it was exposed to the heat shield.

When compared to virgin powder, the chemical examination of spatter particles covered with condensates revealed an increase in oxygen concentration of around 17 times. The condensate on the spatter surface was subjected to an EDS examination, which revealed that the condensate is mostly made up of Cr-based oxide. Thus, it can be said that in the case of Alloy 718, Cr is one of the main sublimating elements. Monitoring of the Cr concentration in both the remaining powder and the manufactured parts is essential due to the significance of Cr for corrosion and high-temperature oxidation resistance for Alloy 718 components. In conclusion, our study reveals that the PBF-EB process's sublimation might be a possible mechanism for the deterioration of powders and manufactured components.

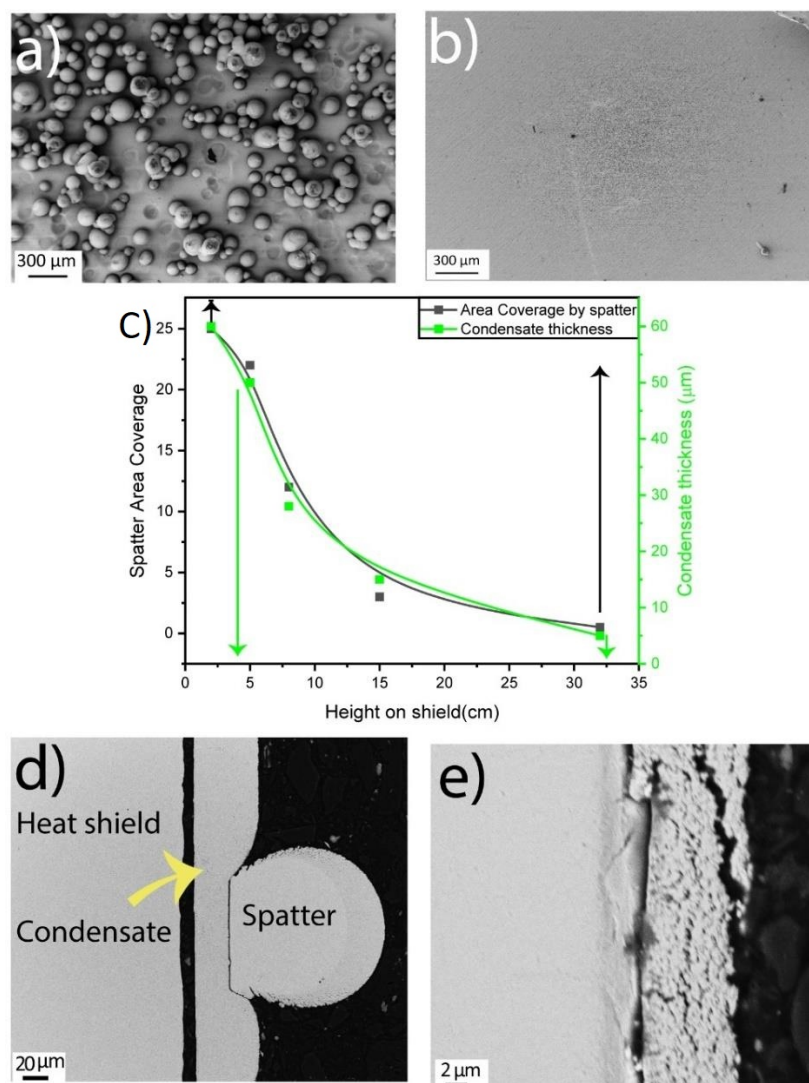


Figure 33: The top micrographs show an area covered by spatters from the a) bottom (2 cm) and b) top (~32 cm) of the heat shield. The center plot c) shows the variation in area coverage by spattering particles and condensate thickness with height on the heat shield. The bottom micrographs show the condensate thickness d) at the bottom (2 cm) and e) top (32 cm) of the heat shield.

8 Conclusions

RQ1: What is the dominant powder degradation mechanism in the PBF-LB process?

- The comprehensive study on the reusability of AlSi10Mg for a prolonged period of 30 months showed that the spatter formation is the main powder degradation mechanism in the PBF-LB process. This was further confirmed by other alloy systems in this thesis, namely Ni-base alloys (HX, Alloy 718) and TiAl6V4.
- For AlSi10Mg powder, the surface of spatter particles was wholly covered with a nodular oxide scale. However, for Ni-based superalloys (HX, Alloy 718), the surface of the spatter particles was covered with oxide particulates and patches. In the case of TiAl6V4, the spatter particle surface was covered with fine oxide particulates enriched with Al-based oxides.
- Analysis of spatters from different materials verified that the spatters are the dominant degradation mechanism in the PBF-LB process, where the extent of spatter oxidation and surface oxide chemistry greatly varies depending upon the composition of the alloy and processing parameters.

RQ2: What is the effect of part geometry and processing parameters on the generation and properties of spatter during PBF-LB?

- The geometry effect characterized by specially designed containers showed that the overhang structures and area-to-volume ratio can significantly influence the spatter generation.
 - o The Optical Tomography analysis showed that lattice geometries with a higher surface-to-volume ratio and lattice geometries with larger overhang structures exhibited a higher amount of heat signals which is an indication of a higher amount of spatter generation.
 - o The containers containing lattice geometries with a higher surface-to-volume ratio showed a 49% increase in oxygen content and the container with a larger overhang structure showed a 22 % increase in oxygen content compared to virgin powder. This confirms the incorporation of oxidized spatter particles by redeposition on the powder bed.
- Increase in spatter formation, studied on HX alloy and TiAl6V4 alloys, using different spatter monitoring techniques, showed that:
 - o the number of hot spatters observed by Optical Tomography is increasing with the layer thickness increase, as was shown in the case of PBF-LB processing of Hastelloy X;
 - o the study on TiAl6V4 showed that even though the spatter generation is increasing with increasing layer thickness per layer, the total amount of spatters per build job, including hot and cold spatters, decreases with the increase in layer thickness.
- Processing atmosphere in terms of composition and purity seems to have the highest impact on spatter formation and its characteristics:
 - o the introduction of He can reduce the number of generated spatters by up to 40 % compared to pure Ar atmosphere;

- the pickup of oxygen, nitrogen, and hydrogen was also lower in the He-based gas atmosphere compared to the pure Ar atmosphere;
- rather minor ~30 % increase in oxygen content from virgin to the spatters generated in the atmosphere containing 20 ppm residual oxygen content was registered. When processing at a standard processing atmosphere with 1000 ppm residual oxygen, the increase was about an order of magnitude higher (~300 %);
- the oxide layer thickness analysis by XPS depth profile showed that the oxide patches/particulates thickness on the surface of spatters significantly decreased with oxygen content decrease from ~75 nm at 1000 ppm O₂ to ~15 nm at 20 ppm.

RQ3: What is the effect of powder degradation on the properties of fabricated parts?

- The study on HX alloy showed that the generated spatters can redeposit on the subsequent parts in the powder bed and result in a lack of fusion defects.
- The study on AlSi10Mg alloy showed that spatter accumulation can be detrimental to the properties of fabricated parts as follows:
 - increase in porosity from <0.7 % in case of virgin powder to 3% in the parts fabricated from powder reused for 30 months;
 - oxide scale present on the spatter particles resulted in a lack of cohesion defects and acted as the nuclei for porosity;
 - the tensile strength also decreased by up to 15 % in the parts fabricated from reused powder.

RQ4: What is the dominant powder degradation mechanism in the PBF-EB process?

- Powder oxidation and formation of oxides stable at high temperature (Al, Ti, Cr) was determined as the dominant powder degradation mechanism in the PBF-EB process. Redistribution of oxygen from the less stable oxide on the powder surface is believed to provide source of oxygen.
- Properties related to rheology improved in reused powder compared to virgin powder after PBF-LB processing of Alloy718 allow powder.
- Investigation related to the study on sublimation during the processing of Alloy 718 showed that Al and Cr are the volatile elements prone to sublimation during the PBF-EB processing of this alloy. The monitoring of such elements during processing on PBF-EB is vital to maintain the quality of powder and the fabricated parts.

9 Future work

In this thesis, the dominant powder degradation mechanisms in terms of powder chemistry during PBF processes have been evaluated. Moreover, the influence of process parameters and alloy composition on the extent of spatter oxidation has been assessed. In light of the reported findings in this thesis and published research, several niches can be found where comprehensive research can be potentially beneficial for the further development of the PBF processes. These are presented in further detail below.

Powder degradation, and particularly surface oxidation, can strongly influence printability and can cause porosity and defect formation. Especially, it can be detrimental to the printability of crack-sensitive alloys e.g., Ni-based superalloys (IN738, IN939, etc.), and Al alloys. There is a need of investigating the effect of powder oxidation and spatter accumulation on crack formation during the printing of such alloys. This can be achieved by a careful analysis of the type of oxides present on the surface of powder/spatter particles and connecting it to the type of oxides present on the surface of cracks in the built sample. In addition, the effect of processing atmosphere purity in restricting the extent of surface oxidation and its role in mitigating the problem of crack formation by the surface oxides will be interesting to evaluate.

Another important aspect that is missing is the thorough investigation of powder degradation on the dynamic properties of the fabricated parts. The results have shown that powder oxidation and spatter accumulation during the PBF-LB process can result in increasing porosity and creating a lack of fusion defects. These defects might not influence the static properties sufficiently but can have a severe effect on the fatigue properties of the fabricated parts. A systematically designed study with proper traceability of the powders during the build can provide a solid base to correlate the fatigue properties with powder reusability.

Sublimation of some critical elements during the PBF-EB process as e.g., Al and Cr from Alloy 718, can influence the properties of the built part. One of the important aspects to analyze is the variation in corrosion characteristics of the printed part in the PBF-EB process compared to the cast part. Additionally, during the powder degradation analysis of alloy 718, it has been found that Al is one of the dominantly oxidized elements which is an element critical for the formation of γ' phase formation. There is a need for a well-designed study combined with appropriate post-processing heat treatment to evaluate the effect of powder degradation on the volume fraction of γ' phase formation in the alloy. With the new superalloys being developed with higher volume fraction of γ' phase, and susceptibility of Al and Ti for oxidation, which are the main γ' phase forming elements, such investigation will be ever more needed.

Additionally, to track the powder degradation with reusability in large industries, there is a need to connect the results from sophisticated surface-sensitive techniques as e.g., XPS, AES, and HRSEM, to more industry-viable characterization techniques e.g., oxygen content, rheological properties of powders, etc. This can be done by standardizing the change in oxygen content and flowability behavior of the powders with reusability against the morphology and surface chemistry of the powder. Such standardization will help to swiftly determine the level of powder degradation and its applicability for a specific application.

Finally, there has been some development regarding the grading of powders depending on the oxygen content in the bulk composition, particularly for TiAl6V4 alloys. This helps to evaluate the suitability of a particular powder for the desired component. There is a need of spreading

this grading standard for all the AM materials, this can help to move the usage of degraded powder from a critical component to a less dynamically critical component, which will eventually increase the powder reusability and increase the sustainability of the process.

10 Acknowledgements

This work was conducted within the framework of the Centre for Additive Manufacturing – Metal (CAM²), supported by the Swedish Governmental Agency of Innovation Systems (Vinnova).

I would like to thank my supervisor Prof. Eduard Hryha and examiner Prof. Lars Nyborg for providing me with this opportunity to explore an interesting dimension of additive manufacturing. Additionally, I would like to express my gratitude to Prof. Eduard Hryha for his guidance and untiring support.

Thanks to Dr. Camille Puzon for her mentorship, collaboration, and many corrections in manuscripts. Also, I appreciate the support, contribution, and collaboration of other co-authors particularly Tobias Fiegl from FAU Erlangen, Germany, Dr. Z. Chen, Claudia Schwerz, and Sophie Dubiez-Le Goff. Furthermore, I would like to thank Andreas Markström for his support in Thermo-Calc-related calculations.

Dr. Eric Tam deserves special thanks for teaching me the XPS technique, tolerating my mistakes, and answering my unending streak of questions about it. Additionally, I would also express my appreciation for Dr. Yiming Yao, Dr. Yu Cao, Engr. Roger Sagdahl, and Jessica Twedmark for their support during this time.

Thanks to all the colleagues in the Department of Industrial and Materials Science who made me feel at home. Special thanks to my AM/PM group colleagues, my roommates at conferences Bala and Fardan, and my officemates Valentina, Laura, and Philip for sharing ideas and discussions. A shout-out to Dmitri Riabov for making bulk chemical analysis possible from Höganäs.

Lastly, I would like to acknowledge my wife, Atiqa, and parents for their support and patience.

11 References

- [1] P. Novák, *Advanced powder metallurgy technologies*, 2020. <https://doi.org/10.3390/ma13071742>.
- [2] W.B. James, *Powder Metallurgy Methods and Applications*, *Powder Metall.* 7 (2018) 9–19. <https://doi.org/10.31399/asm.hb.v07.a0006022>.
- [3] A. Raza, S. Abdulahad, B. Kang, H.J. Ryu, S.H. Hong, Corrosion resistance of weight reduced Al x CrFeMoV high entropy alloys, *Appl. Surf. Sci.* 485 (2019) 368–374. <https://doi.org/10.1016/j.apsusc.2019.03.173>.
- [4] B. Kang, J. Lee, H. Jin, S. Hyung, H.J. Ryu, S.H. Hong, Ultra-high strength WNbMoTaV high-entropy alloys with fine grain structure fabricated by powder metallurgical process, *Mater. Sci. Eng. A.* 712 (2017) 616–624. <https://doi.org/10.1016/j.msea.2017.12.021>.
- [5] A. Raza, B. Kang, J. Lee, H.J. Ryu, S.H. Hong, Transition in microstructural and mechanical behavior by reduction of sigma-forming element content in a novel high entropy alloy, *Mater. Des.* 145 (2018) 11–19. <https://doi.org/10.1016/j.matdes.2018.02.036>.
- [6] A. Raza, H. Jin, S. Hyung, Strength enhancement and density reduction by the addition of Al in CrFeMoV based high-entropy alloy fabricated through powder metallurgy, *Mater. Des.* 157 (2018) 97–104. <https://doi.org/10.1016/j.matdes.2018.07.023>.
- [7] S. Brischetto, P. Maggiore, C.G. Ferro, *Additive Manufacturing Technologies and Applications*, MDPI, 2018. <https://doi.org/10.3390/books978-3-03842-549-6>.
- [8] J.H. Martin, B.D. Yahata, J.M. Hundley, J.A. Mayer, T.A. Schaedler, T.M. Pollock, 3D printing of high-strength aluminium alloys, *Nature.* 549 (2017) 365–369. <https://doi.org/10.1038/nature23894>.
- [9] M. Munsch, M. Schmidt-Lehr, E. Wycisk, T. Führer, *AMPOWER Report 2022*, 2022.
- [10] A. Raza, *Powder degradation during powder bed fusion processing*, Thesis. (2021).
- [11] Z. Chen, A. Raza, E. Hryha, Influence of part geometry on spatter formation in laser powder bed fusion of Inconel 718 alloy revealed by optical tomography, *J. Manuf. Process.* 81 (2022) 680–695. <https://doi.org/10.1016/j.jmapro.2022.07.031>.
- [12] L. Cordova, A. Raza, E. Hryha, *Rheological Behavior of Inconel 718 Powder for Electron-Beam Melting*, Metals (Basel). (2022).
- [13] A. Raza, T. Fiegl, I. Hanif, A. Markström, M. Franke, C. Körner, E. Hryha, Degradation of AlSi10Mg powder during laser based powder bed fusion processing, *Mater. Des.* 198 (2021) 109358. <https://doi.org/10.1016/j.matdes.2020.109358>.
- [14] H. Gruber, M. Henriksson, E. Hryha, L. Nyborg, Effect of Powder Recycling in Electron Beam Melting on the Surface Chemistry of Alloy 718 Powder, *Metall. Mater. Trans. A Phys. Metall. Mater. Sci.* 50 (2019) 4410–4422. <https://doi.org/10.1007/s11661-019-05333-7>.
- [15] C. Pauzon, P. Forêt, E. Hryha, T. Arunprasad, L. Nyborg, Argon-helium mixtures as Laser-Powder Bed Fusion atmospheres: Towards increased build rate of Ti-6Al-4V, *J. Mater. Process. Technol.* 279 (2020) 116555. <https://doi.org/10.1016/j.jmatprotec.2019.116555>.

- [16] A. Raza, C. Pauzon, E. Hryha, A. Markström, P. Forêt, Spatter oxidation during laser powder bed fusion of Alloy 718: dependence on oxygen content in the process atmosphere, *Addit. Manuf.* 48 (2021) 102369. <https://doi.org/10.1016/j.addma.2021.102369>.
- [17] A. Raza, Characterization of Spatter and Sublimation in Alloy 718 during Electron Beam Melting Ahmad, *Materials (Basel)*. 15 (2021). <https://doi.org/https://doi.org/10.3390/ma14205953>.
- [18] L. Dowling, J. Kennedy, S. O'Shaughnessy, D. Trimble, A review of critical repeatability and reproducibility issues in powder bed fusion, *Mater. Des.* 186 (2020) 108346. <https://doi.org/10.1016/j.matdes.2019.108346>.
- [19] C. Schwerz, A. Raza, X. Lei, L. Nyborg, E. Hryha, H. Wirdelius, In-situ detection of redeposited spatter and its influence on the formation of internal flaws in laser powder bed fusion, *Addit. Manuf.* 47 (2021) 102370. <https://doi.org/10.1016/j.addma.2021.102370>.
- [20] C. Pauzon, A. Raza, E. Hryha, P. Forêt, Oxygen balance during laser powder bed fusion of Alloy 718, *Mater. Des.* 201 (2021). <https://doi.org/10.1016/j.matdes.2021.109511>.
- [21] C. Pauzon, A. Markström, S.D. Goff, E. Hryha, Effect of the Process Atmosphere Composition on Alloy 718 Produced by Laser Powder Bed Fusion, (2021).
- [22] S. Vock, B. Klöden, A. Kirchner, T. Weißgärber, B. Kieback, Powders for powder bed fusion: a review, *Prog. Addit. Manuf.* 4 (2019) 383–397. <https://doi.org/10.1007/s40964-019-00078-6>.
- [23] L. Cordova, T. Bor, M. de Smit, M. Campos, T. Tinga, Measuring the spreadability of pre-treated and moisturized powders for laser powder bed fusion, *Addit. Manuf.* 32 (2020) 101082. <https://doi.org/10.1016/j.addma.2020.101082>.
- [24] A.T. Sutton, C.S. Kriewall, S. Karnati, M.C. Leu, J.W. Newkirk, Characterization of AISI 304L stainless steel powder recycled in the laser powder-bed fusion process, *Addit. Manuf.* 32 (2020) 100981. <https://doi.org/10.1016/j.addma.2019.100981>.
- [25] O.A. Quintana, J. Alvarez, R. Mcmillan, W. Tong, C. Tomonto, Effects of Reusing Ti-6Al-4V Powder in a Selective Laser Melting Additive System Operated in an Industrial Setting, *Jom.* 70 (2018) 1863–1869. <https://doi.org/10.1007/s11837-018-3011-0>.
- [26] A. Gebhardt, J.-H. Steffen, Additive manufacturing (3D printing) for analytical chemistry, *Book.* 3 (2021). <https://doi.org/10.1016/j.talo.2021.100036>.
- [27] I. Gibson, D. Rosen, B. Stucker, M. Khorasani, *Additive Manufacturing Technologies*, 2020. <https://doi.org/10.2207/jjws.89.82>.
- [28] L.C. Zhang, Y. Liu, S. Li, Y. Hao, Additive Manufacturing of Titanium Alloys by Electron Beam Melting: A Review, *Adv. Eng. Mater.* 20 (2018) 1–16. <https://doi.org/10.1002/adem.201700842>.
- [29] J. Schwerdtfeger, C. Körner, Selective electron beam melting of Ti-48Al-2Nb-2Cr: Microstructure and aluminium loss, *Intermetallics.* 49 (2014) 29–35. <https://doi.org/10.1016/j.intermet.2014.01.004>.

- [30] E. Hryha, D. Riabov, Metal Powder Production for Additive Manufacturing, *Encycl. Mater. Met. Alloys*. 3 (2022) 264–271. <https://doi.org/10.1016/b978-0-12-819726-4.00089-2>.
- [31] S.E. Brika, M. Letenneur, C.A. Dion, V. Brailovski, Influence of particle morphology and size distribution on the powder flowability and laser powder bed fusion manufacturability of Ti-6Al-4V alloy, *Addit. Manuf.* 31 (2020) 100929. <https://doi.org/10.1016/j.addma.2019.100929>.
- [32] J.J. Dunkley, Metal powder atomisation methods for modern manufacturing, *Johnson Matthey Technol. Rev.* 63 (2019) 226–232. <https://doi.org/10.1595/205651319X15583434137356>.
- [33] C.F. Dixon, Atomizing molten metals—a review, *Can. Metall. Q.* 12 (1973) 309–321. <https://doi.org/10.1179/cmq.1973.12.3.309>.
- [34] L.V.M. Antony, R.G. Reddy, Processes for production of high-purity metal powders, *Jom.* 55 (2003) 14–18. <https://doi.org/10.1007/s11837-003-0153-4>.
- [35] D. Riabov, E. Hryha, M. Rashidi, S. Bengtsson, L. Nyborg, Effect of atomization on surface oxide composition in 316L stainless steel powders for additive manufacturing, *Surf. Interface Anal.* 52 (2020) 694–706. <https://doi.org/10.1002/sia.6846>.
- [36] M. Entezarian, F. Allaire, P. Tsantrizos, R.A.L. Drew, Plasma atomization: A new process for the production of fine, spherical powders, *Jom.* 48 (1996) 53–55. <https://doi.org/10.1007/BF03222969>.
- [37] A. Strondl, O. Lyckfeldt, H. Brodin, U. Ackelid, Characterization and Control of Powder Properties for Additive Manufacturing, *Jom.* 67 (2015) 549–554. <https://doi.org/10.1007/s11837-015-1304-0>.
- [38] J.A. Slotwinski, E.J. Garboczi, P.E. Stutzman, C.F. Ferraris, S.S. Watson, M.A. Peltz, Characterization of metal powders used for additive manufacturing, *J. Res. Natl. Inst. Stand. Technol.* 119 (2014) 460–493. <https://doi.org/10.6028/jres.119.018>.
- [39] A. Mussatto, R. Groarke, A. O’Neill, M.A. Obeidi, Y. Delaure, D. Brabazon, Influences of powder morphology and spreading parameters on the powder bed topography uniformity in powder bed fusion metal additive manufacturing, *Addit. Manuf.* 38 (2021) 101807. <https://doi.org/10.1016/j.addma.2020.101807>.
- [40] A.T. Sutton, C.S. Kriewall, M.C. Leu, J.W. Newkirk, Powders for additive manufacturing processes: Characterization techniques and effects on part properties, *Solid Free. Fabr. 2016 Proc. 27th Annu. Int. Solid Free. Fabr. Symp. - An Addit. Manuf. Conf. SFF 2016.* (2016) 1004–1030.
- [41] A. Averardi, C. Cola, S.E. Zeltmann, N. Gupta, Effect of particle size distribution on the packing of powder beds: A critical discussion relevant to additive manufacturing, *Mater. Today Commun.* 24 (2020) 100964. <https://doi.org/10.1016/j.mtcomm.2020.100964>.
- [42] G. Shanbhag, M. Vlasea, Powder Reuse Cycles in Electron Beam Powder Bed Fusion—Variation of Powder Characteristics, *Materials (Basel)*. 14 (2021) 4602. <https://doi.org/10.3390/ma14164602>.
- [43] F. Ahmed, U. Ali, D. Sarker, E. Marzbanrad, K. Choi, Y. Mahmoodkhani, E. Toyserkani, Study of powder recycling and its effect on printed parts during laser

- powder-bed fusion of 17-4 PH stainless steel, *J. Mater. Process. Technol.* 278 (2020) 116522. <https://doi.org/10.1016/j.jmatprotec.2019.116522>.
- [44] A. Sergi, R.H.U. Khan, M.M. Attallah, The role of powder atomisation route on the microstructure and mechanical properties of hot isostatically pressed Inconel 625, *Mater. Sci. Eng. A.* 808 (2021) 140950. <https://doi.org/10.1016/j.msea.2021.140950>.
- [45] H. Gruber, C. Luchian, E. Hryha, L. Nyborg, Effect of Powder Recycling on Defect Formation in Electron Beam Melted Alloy 718, *Metall. Mater. Trans. A Phys. Metall. Mater. Sci.* 51 (2020) 2430–2443. <https://doi.org/10.1007/s11661-020-05674-8>.
- [46] L. Cordova, M. Campos, T. Tinga, Revealing the Effects of Powder Reuse for Selective Laser Melting by Powder Characterization, *JOM.* 71 (2019) 1062–1072. <https://doi.org/10.1007/s11837-018-3305-2>.
- [47] A.T. Sutton, C.S. Kriewall, M.C. Leu, J.W. Newkirk, B. Brown, Characterization of laser spatter and condensate generated during the selective laser melting of 304L stainless steel powder, *Addit. Manuf.* 31 (2020) 100904. <https://doi.org/10.1016/j.addma.2019.100904>.
- [48] E. Hryha, E. Dudrova, L. Nyborg, On-line control of processing atmospheres for proper sintering of oxidation-sensitive PM steels, *J. Mater. Process. Technol.* 212 (2012) 977–987. <https://doi.org/10.1016/j.jmatprotec.2011.12.008>.
- [49] M. Skalon, B. Meier, T. Leitner, S. Arneitz, S.T. Amancio-Filho, C. Sommitsch, Reuse of Ti6Al4V powder and its impact on surface tension, melt pool behavior and mechanical properties of additively manufactured components, *Materials (Basel)*. 14 (2021) 1–22. <https://doi.org/10.3390/ma14051251>.
- [50] L.C. Ardila, F. Garcíandia, J.B. González-Díaz, P. Álvarez, A. Echeverría, M.M. Petite, R. Deffley, J. Ochoa, Effect of IN718 recycled powder reuse on properties of parts manufactured by means of Selective Laser Melting, in: *Phys. Procedia*, Elsevier B.V., 2014: pp. 99–107. <https://doi.org/10.1016/j.phpro.2014.08.152>.
- [51] C. Pauzon, B. Hoppe, T. Pichler, S. Dubiez-Le Goff, P. Forêt, T. Nguyen, E. Hryha, Reduction of incandescent spatter with helium addition to the process gas during laser powder bed fusion of Ti-6Al-4V, *CIRP J. Manuf. Sci. Technol.* 35 (2021) 371–378. <https://doi.org/10.1016/j.cirpj.2021.07.004>.
- [52] J. Yin, L.L. Yang, X. Yang, H. Zhu, D. Wang, L. Ke, Z. Wang, G. Wang, X. Zeng, High-power laser-matter interaction during laser powder bed fusion, *Addit. Manuf.* 29 (2019) 100778. <https://doi.org/10.1016/j.addma.2019.100778>.
- [53] Z.A. Young, Q. Guo, N.D. Parab, C. Zhao, M. Qu, L.I. Escano, K. Fezzaa, W. Everhart, T. Sun, L. Chen, Types of spatter and their features and formation mechanisms in laser powder bed fusion additive manufacturing process, *Addit. Manuf.* 36 (2020) 101438. <https://doi.org/10.1016/j.addma.2020.101438>.
- [54] T. Özel, Y.M. Arisoy, L.E. Criales, Computational simulation of thermal and spattering phenomena and microstructure in selective laser melting of inconel 625, in: *Phys. Procedia*, 2016: pp. 1435–1443. <https://doi.org/10.1016/j.phpro.2016.08.149>.
- [55] M. Simonelli, C. Tuck, N.T. Aboulkhair, I. Maskery, I. Ashcroft, R.D. Wildman, R. Hague, A Study on the Laser Spatter and the Oxidation Reactions During Selective Laser Melting of 316L Stainless Steel, Al-Si10-Mg, and Ti-6Al-4V, *Metall. Mater.*

- Trans. A Phys. Metall. Mater. Sci. 46 (2015) 3842–3851.
<https://doi.org/10.1007/s11661-015-2882-8>.
- [56] Y. Liu, Y. Yang, S. Mai, D. Wang, C. Song, Investigation into spatter behavior during selective laser melting of AISI 316L stainless steel powder, *Mater. Des.* 87 (2015) 797–806. <https://doi.org/10.1016/j.matdes.2015.08.086>.
- [57] S. Ly, A.M. Rubenchik, S.A. Khairallah, G. Guss, M.J. Matthews, Metal vapor micro-jet controls material redistribution in laser powder bed fusion additive manufacturing, *Sci. Rep.* 7 (2017) 1–12. <https://doi.org/10.1038/s41598-017-04237-z>.
- [58] S.A. Khairallah, A.T. Anderson, A. Rubenchik, W.E. King, Laser powder-bed fusion additive manufacturing: Physics of complex melt flow and formation mechanisms of pores, spatter, and denudation zones, *Acta Mater.* 108 (2016) 36–45. <https://doi.org/10.1016/j.actamat.2016.02.014>.
- [59] P. Moghimian, T. Poirié, M. Habibnejad-Korayem, J.A. Zavala, J. Kroeger, F. Marion, F. Larouche, Metal powders in additive manufacturing: A review on reusability and recyclability of common titanium, nickel and aluminum alloys, *Addit. Manuf.* 43 (2021). <https://doi.org/10.1016/j.addma.2021.102017>.
- [60] V. Gunenthiram, P. Peyre, M. Schneider, M. Dal, F. Coste, I. Koutiri, R. Fabbro, Experimental analysis of spatter generation and melt-pool behavior during the powder bed laser beam melting process, *J. Mater. Process. Technol.* 251 (2018) 376–386. <https://doi.org/10.1016/j.jmatprotec.2017.08.012>.
- [61] M.J. Heiden, L.A. Deibler, J.M. Rodelas, J.R. Koepke, D.J. Tung, D.J. Saiz, B.H. Jared, Evolution of 316L stainless steel feedstock due to laser powder bed fusion process, *Addit. Manuf.* 25 (2019) 84–103. <https://doi.org/10.1016/j.addma.2018.10.019>.
- [62] T. Fiegl, M. Franke, A. Raza, E. Hryha, C. Körner, Effect of AlSi10Mg0.4 long-term reused powder in PBF-LB/M on the mechanical properties, *Mater. Des.* 212 (2021) 110176. <https://doi.org/10.1016/j.matdes.2021.110176>.
- [63] S. Ghods, E. Schultz, C. Wisdom, R. Schur, R. Pahuja, A. Montelione, D. Arola, M. Ramulu, Electron beam additive manufacturing of Ti6Al4V: Evolution of powder morphology and part microstructure with powder reuse, *Materialia*. 9 (2020) 100631. <https://doi.org/10.1016/j.mtla.2020.100631>.
- [64] A. Montelione, S. Ghods, R. Schur, C. Wisdom, D. Arola, M. Ramulu, Powder Reuse in Electron Beam Melting Additive Manufacturing of Ti6Al4V: Particle Microstructure, Oxygen Content and Mechanical Properties, *Addit. Manuf.* 35 (2020) 101216. <https://doi.org/10.1016/j.addma.2020.101216>.
- [65] .E.L. Peeyush Nandwana, William H. Peter, Ryan R. Dehoff, And S.S.B. Michael M. Kirka, Francisco Medina, Recyclability Study on Inconel 718 and Ti-6Al-4V Powders for Use in Electron Beam Melting, *Metall. Mater. Trans. B.* 47 (2016) 754–762. <https://doi.org/10.1007/s10884-015-9497-z>.
- [66] G. Shanbhag, M. Vlasea, The effect of reuse cycles on Ti-6Al-4V powder properties processed by electron beam powder bed fusion, *Manuf. Lett.* 25 (2020) 60–63. <https://doi.org/10.1016/j.mfglet.2020.07.007>.
- [67] S. Chandrasekar, J.B. Coble, S. Yoder, P. Nandwana, R.R. Dehoff, V.C. Paquit, S.S.

- Babu, Investigating the effect of metal powder recycling in Electron beam Powder Bed Fusion using process log data, *Addit. Manuf.* 32 (2020).
<https://doi.org/10.1016/j.addma.2019.100994>.
- [68] Y. Sun, M. Aindow, R.J. Hebert, The effect of recycling on the oxygen distribution in Ti-6Al-4V powder for additive manufacturing, *Mater. High Temp.* 35 (2018) 217–224.
<https://doi.org/10.1080/09603409.2017.1389133>.
- [69] V. Juechter, T. Scharowsky, R.F. Singer, C. Körner, Processing window and evaporation phenomena for Ti-6Al-4V produced by selective electron beam melting, *Acta Mater.* 76 (2014) 252–258. <https://doi.org/10.1016/j.actamat.2014.05.037>.
- [70] D. Cormier, O. Harrysson, T. Mahale, H. West, Freeform Fabrication of Titanium Aluminide via Electron Beam Melting Using Prealloyed and Blended Powders, *Res. Lett. Mater. Sci.* 2007 (2007) 1–4. <https://doi.org/10.1155/2007/34737>.
- [71] V. Petrovic, R. Niñerola, Powder recyclability in electron beam melting for aeronautical use, *Aircr. Eng. Aerosp. Technol.* 87 (2015) 147–155.
<https://doi.org/10.1108/AEAT-11-2013-0212>.
- [72] E. Damri, E. Tiferet, D. Braun, Y.I. Ganor, M. Chonin, I. Orion, Effects of gas pressure during electron beam energy deposition in the ebm additive manufacturing process, *Metals (Basel)*. 11 (2021) 1–13. <https://doi.org/10.3390/met11040601>.
- [73] C. GRARD, Aluminium and its alloys, Ebook. (n.d.).
<https://doi.org/10.1002/jctb.5000391304>.
- [74] H.R. Kotadia, G. Gibbons, A. Das, P.D. Howes, A review of Laser Powder Bed Fusion Additive Manufacturing of aluminium alloys: Microstructure and properties, *Addit. Manuf.* 46 (2021) 102155. <https://doi.org/10.1016/j.addma.2021.102155>.
- [75] N.T. Aboulkhair, M. Simonelli, L. Parry, I. Ashcroft, C. Tuck, R. Hague, 3D printing of Aluminium alloys: Additive Manufacturing of Aluminium alloys using selective laser melting, *Prog. Mater. Sci.* 106 (2019) 100578.
<https://doi.org/10.1016/j.pmatsci.2019.100578>.
- [76] P.A. Rometsch, Y. Zhu, X. Wu, A. Huang, Review of high-strength aluminium alloys for additive manufacturing by laser powder bed fusion, *Mater. Des.* 219 (2022) 110779. <https://doi.org/10.1016/j.matdes.2022.110779>.
- [77] N. Minhas, V. Sharma, S.S. Bhadauria, A review on weldability and corrosion behaviour of L-PBF printed AlSi10Mg alloy, *Can. Metall. Q.* (2022) 1–33.
<https://doi.org/10.1080/00084433.2022.2111968>.
- [78] K. Kempen, L. Thijs, J. Van Humbeeck, J.P. Kruth, Processing AlSi10Mg by selective laser melting: Parameter optimisation and material characterisation, *Mater. Sci. Technol.* 31 (2015) 917–923. <https://doi.org/10.1179/1743284714Y.0000000702>.
- [79] R.C. Reed, *The Superalloys as High-Temperature Materials*, 2006.
- [80] S. Tin, *Superalloy2020*, 2020.
- [81] J. Andersson, Welding metallurgy and weldability of superalloys, *Metals (Basel)*. 10 (2020) 3–5. <https://doi.org/10.3390/met10010143>.
- [82] M.C. Chaturvedi, Y.F. Han, Strengthening mechanisms in Inconel 718 superalloy,

- Met. Sci. 17 (1983) 1–5. <https://doi.org/10.1179/030634583790421032>.
- [83] S. Sanchez, P. Smith, Z. Xu, G. Gaspard, C.J. Hyde, W.W. Wits, I.A. Ashcroft, H. Chen, A.T. Clare, Powder Bed Fusion of nickel-based superalloys: A review, *Int. J. Mach. Tools Manuf.* 165 (2021). <https://doi.org/10.1016/j.ijmachtools.2021.103729>.
- [84] ASM, Titanium and its Alloys, *Adv. AMaterials Process.* (2008) 2008.
- [85] S. Liu, Y.C. Shin, Additive manufacturing of Ti6Al4V alloy: A review, *Mater. Des.* 164 (2019) 107552. <https://doi.org/10.1016/j.matdes.2018.107552>.
- [86] T. Zhang, C.-T. Liu, Design of titanium alloys by additive manufacturing: A critical review, *Adv. Powder Mater.* 1 (2022) 100014. <https://doi.org/10.1016/j.apmate.2021.11.001>.
- [87] N. Brodusch, H. Demers, R. Gauvin, *Field Emission Scanning Electron Microscopy.*, 2018.
- [88] A. Ul-Hamid, *A Beginners' Guide to Scanning Electron Microscopy*, 2018. <https://doi.org/10.1007/978-3-319-98482-7>.
- [89] C. Oikonomou, D. Nikas, E. Hryha, L. Nyborg, Evaluation of the thickness and roughness of homogeneous surface layers on spherical and irregular powder particles, *Surf. Interface Anal.* 46 (2014) 1028–1032. <https://doi.org/10.1002/sia.5439>.
- [90] C. Oikonomou, E. Hryha, L. Nyborg, Development of methodology for surface analysis of soft magnetic composite powders, *Surf. Interface Anal.* 44 (2012) 1166–1170. <https://doi.org/10.1002/sia.3848>.
- [91] B.A. Taleatu, E. Omotoso, C. Lal, W.O. Makinde, K.T. Ogundele, E. Ajenifuja, A.R. Lasisi, M.A. Eleruja, G.T. Mola, XPS and some surface characterizations of electrodeposited MgO nanostructure, *Surf. Interface Anal.* 46 (2014) 372–377. <https://doi.org/10.1002/sia.5425>.
- [92] J.F. Moulder, W.F. Stickle, P.E. Sobol, K.D. Bomben, *Handbook of X-ray photoelectron spectroscopy: a reference book of standard spectra for identification and interpretation of XPS data*; Physical Electronics: Eden Prairie, MN, 1995, (2000) 261. <https://www.cnyn.unam.mx/~wencel/XPS/MANXPS.pdf>.

